Oil Spill Timely Backtracking Oriented by Wind Field Correction With Self-Attention Temporal Convolutional Networks

Yongqing Li, Xinrong Lyu, and Peng Ren, *Senior Member, IEEE*

***Abstract*—We investigate the problem of oil spill timely backtracking. Most existing methods for backtracking oil spills rely heavily on historical wind fields. However, during the crucial early stages of an oil spill accident, only inaccurate forecasted or observed wind fields are available as historical data, which do not guarantee reliable accuracy for backtracking the oil spills. On the other hand, reanalysis wind fields are more accurate data for the historical wind fields. However, they normally have a latency of many days and can hardly be used for backtracking the oil spills in a timely manner. To obtain a timely and accurate estimate of the historical wind fields, we develop a self-attention temporal convolutional network (SaTCN). The SaTCN consists of a self-attention network and a temporal convolutional network. The self-attention network captures spatial correlations from a historical wind field sequence in a global manner. The temporal convolutional network captures spatial correlations and temporal characteristics from an attention-weighted wind field sequence in a local manner. The SaTCN is trained subject to the differences between the timely but inaccurate data of both forecasted and observed wind fields and the accurate but delayed data of reanalysis wind fields. The well-trained SaTCN can correct the timely historical wind fields into more accurate ones by approximating the reanalysis wind fields. The corrected historical wind fields thus obtained enable timely, accurate oil spill backtracking. Extensive experiments validate the effectiveness of the proposed backtracking method in addressing the Sanchi and Symphony oil spill accidents.**

***Index Terms*—Oil spill backtracking, self-attention, temporal convolutional network, wind field correction.**

I. Introduction

OIL spills are typical pollution to the oceanic environment and have a significant impact on the sustainable development of oceanic economies [1], [2], [3], [4], [5]. After obtaining the location of an oil spill via remote sensing [6], one way to mitigate the extent of oil spill contamination in time is to backtrack the source of the spill in a timely manner. As wind [7] is one major factor for driving oil spill drifts, high-quality data for the wind plays an important role in oil spill timely backtracking. In the subsequent parts of this section, we review both existing oil spill backtracking methods and existing wind field correction methods. We propose a novel strategy for timely backtracking oil spills using deep learning, and highlight the unique contributions of our research.

A. Review of Oil Spill Backtracking

Oil spill backtracking has been studied for decades [8], [9]. Many operational oil spill backtracking models have been developed to serve specific regions [10], [11]. Seatrack Web is a fully operational oil spill backtracking system that employs automatic identification system (AIS) ship track data [12]. The system has been utilized to retroactively identify potential vessels responsible for oil spills in the Baltic Sea, a portion of the North Sea, and the Gulf of Finland [13]. An OILMAP oil spill model was configured to incorporate meteorological and hydrodynamic data services for the coastal regions of Dubai [14]. The model utilizes a deterministic approach for conducting oil spill backtracking, which allows for the determination of oil spill sources, as well as the identification of intentional discharges. A TESEO oil spill transport model was employed for the purpose of conducting backward simulations of buoys through the utilization of high-frequency (HF) radar currents [15], [16]. Upon utilizing HF radar currents as inputs, the model is able to output more accurate simulated trajectories as compared to simulations that utilize numerical currents. A numerical model BOil was developed for oil spill backtracking in the Kuwaiti offshore and Arabian Gulf waters [17]. The BOil model was coupled with a hydrodynamic numerical model KGulf and can be operated on a smart mobile. An operational backtracking system developed for the Iberia coast [18] integrated CleanSeaNet oil spill detections and ship trajectories supplied by AIS. It can provide efficient backtracking results and has been validated by multiple satellite observations. An operational backtracking system was investigated for the northwest European shelf sea [19]. The system integrates an open modal analysis (OMA) model, providing HF radar surface currents and an oil spill transport model named

Manuscript received 27 January 2023; revised 31 May 2023 and 24 August 2023; accepted 5 September 2023. Date of publication 9 November 2023; date of current version 8 February 2024. This work was supported in part by the National Natural Science Foundation of China under Project 61971444, in part by Taishan Scholar Project, and in part by the Innovative Research Team Program for Young Scholars at Universities in Shandong Province under Project 2020KJN010. *(Corresponding author: Peng Ren.)*

Associate Editor: M. Haller.

Yongqing Li is with the College of Control Science and Engineering, China University of Petroleum (East China), Qingdao 266580, China (e-mail: lyq_upc@163.com).

Xinrong Lyu and Peng Ren are with the College of Oceanography and Space Informatics, China University of Petroleum (East China), Qingdao 266580, China (e-mail: lvxr@upc.edu.cn; pengren@upc.edu.cn).

Digital Object Identifier 10.1109/JOE.2023.3314101

TABLE I
TIMELINESS DESCRIPTIONS OF REANALYSIS WIND FIELDS

Institution	Product	Time of latency
NCEP/NCAR	Reanalysis-1	24 days
NCEP/DOE	Reanalysis-2	24 days
ECMWF	ERA5	5 days

TESEO. The backtracking results with the OMA currents are more accurate than those with currents from a hydrodynamic model.

Some recent oil spill backtracking studies were conducted to address specific difficulties. A backtracking investigation of Deepwater Horizon oil spill accident was conducted to analyze the oil spill impacts on sea turtles across the Atlantic [20]. A modified Lagrangian model was utilized to locate the oil spill positions for PL19-3 oil spill accident that occurred in the Bohai Sea [21], where wind velocity, current velocity, Stokes drift velocity, and turbulent diffusive velocity were linearly combined to simulate the oil particle movements. A numerical backtracking model was used to locate the source of tar balls depositing along the west coast of India [22]. The backtracking results confirmed that the tar balls deposited in different years were derived from the tanker routes and the Bombay High oil fields separately. A calibrated Lagrangian model was developed with a series of Envisat ASAR images [23]. The calibrated model was configured with optimal parameters for a special oil spill accident. The calibration operations were conducted by minimizing the differences between backtracked and observed oil spill locations. The backtracking results were validated via PL19-3 oil spill accident. An oil spill backtracking method was developed for locating both sea surface oil spill source and underwater oil spill source [24]. The research results reflect that accurate hydrodynamic background fields are important for oil spill backtracking performance and it is feasible to improve the background data by assimilating observation data. A hypothetical oil spill simulation was conducted to investigate the oil spill impact on Cyclades islands with surface winds and currents ranging from 2013 to 2018 [25]. The simulation results showed the islands were at high risk due to their proximity to the main oil tanker routes.

Most existing oil spill backtracking models are driven by two crucial factors, i.e., historical wind fields and historical current fields. The historical current fields are highly related to the historical wind fields. The data for the historical wind fields include forecasted wind fields, observed wind fields, and reanalysis wind fields. In the early stages of an oil spill accident, only the forecasted or observed wind fields are available historical wind field data. However, these data are relatively inaccurate, which limits the accuracy of oil spill backtracking. On the other hand, the reanalysis wind fields are produced by comprehensively integrating the forecasted and observed wind fields with a numerical assimilation system. They are relatively more accurate but are not available in the early stages of the oil spill accident [26]. The timeliness descriptions of the reanalysis wind fields are given in Table I. They normally have latency of many days, which makes them unsuitable for oil spill timely backtracking. In this scenario, obtaining accurate historical wind fields before the availability of reanalysis wind fields is a challenging problem that needs to be addressed for oil spill timely backtracking.

B. *Review of Wind Field Correction*

As discussed at the end of Section I-A, forecasted or observed wind fields have limited accuracy, while reanalysis wind fields are more accurate wind field estimates but with time latency [27]. Wind field correction is an effective way to bridge the inaccurate wind fields and the accurate ones [28]. In recent years, wind speed correction in a single-station fashion was investigated to improve numerically forecasted wind fields. Kalman filtering was used to improve numerical weather predictions by recursively combining observations and numerical forecasts to minimize corresponding biases [29]. Seven adaptive methods for forecasted wind speed correction were discussed and compared based on seven synoptic stations around Ireland [30]. A hybrid method was developed with four mathematical models (i.e., MLR, NLR, ANN, and SVM) to correct forecasted wind speeds derived from a MM5 mesoscale model [31]. An artificial neural network (ANN)-based postprocessing method was developed for improving solar radiation forecasts from a weather forecast mesoscale model [32]. A differential polynomial neural network (DPNN) was developed to correct wind speeds derived from an Aladin numerical forecast model and the National Oceanic and Atmospheric Administration (NOAA) [33]. The DPNN formed general differential equations to model complex systems and was trained as a correction function according to real observations. Three wind speed correction methods were developed based on multiple linear regression, a radial basis function neural network and an Elman neural network [34]. An ANN/SVM-based model was developed to learn relationships between wind speed forecasts and measurements for correcting wind-electric power forecasts [35]. A novel scheme was developed to improve wind measurement accuracy by extracting sea surface wind information from rain-contaminated *X*-band marine radar images [36]. A lightGBM method was developed for correcting numerically forecasted wind speed from ECMWF for 18 observation stations [37]. A short-term wind power prediction model based on ensemble learning was developed, considering the rolling error correction strategy [38]. A wind field correction method was developed to simulate storm surge and inundation based on a finite-volume coastal ocean model (FVCOM), and the method was validated with the typhoon Rammasun [39].

A wind field correction method was developed to correct the forecasted wind fields from the global forecast system (GFS) of National Centres for Environmental Prediction (NCEP) [40]. A wind field correction model named CU-net was developed to correct forecasted wind fields from the European center for medium-range weather forecast integrated forecasting system (ECMWF-IFS) to be those close to reanalysis wind fields from ECMWF-ERA5 [41].

Most existing methods for correcting historical wind fields are based on data from a single station, which limits their ability to capture the spatial characteristics reflected in wind fields. However, wind fields contain more information that is crucial for oil spill backtracking, as the drift of an oil spill is primarily influenced by field forces [42]. Therefore, an accurate correction of historical wind fields is essential for achieving timely and accurate oil spill backtracking.

C. Promising Oil Spill Timely Backtracking Strategy Based on Deep Learning

In recent years, deep learning-based spatial-temporal networks, such as ConvLSTM [43], [44] and temporal convolutional network (TCN) [45] frameworks, have made significant advancements in extracting sequential characteristics. However, the ConvLSTM frameworks have a high computational cost and are not efficient for correcting wind fields. The TCN frameworks are efficient networks but they are primarily used for processing vector sequences with 1-D convolutional neural networks (1DCNNs). They are incapable of extracting 2-D spatial correlations from a wind field sequence in a global manner. Therefore, while deep learning paves a promising way to sequential analysis, the development of deep architecture for wind field correction still remains an open problem.

To achieve accurate and timely oil spill backtracking, we develop a novel deep learning-based method for correcting historical wind fields. This is achieved by utilizing a self-attention temporal convolutional network (SaTCN) to learn the differences between inaccurate and accurate historical wind fields. The SaTCN is composed of a self-attention network and a temporal convolutional network (TCN). Specifically, the TCN is developed to process tensor sequences by utilizing 3-D convolutional neural networks (3DCNNs), which enables it to effectively capture the characteristics of wind field sequences in the form of a tensor. The SaTCN is trained on historical wind fields, including forecasted, observed, and reanalysis wind fields. The SaTCN comprehensively captures both spatial and temporal characteristics of the input wind field sequence. In practical operations, the SaTCN takes forecasted and observed wind fields as input and produces corrected historical wind fields that approximate the reanalysis wind fields.

We utilize the corrected historical wind fields to drive a numerical backtracking model for the purpose of conducting oil spill backtracking in a timely manner. The proposed method for oil spill timely backtracking results in more accurate backtracking outcomes as compared to using the original historical wind fields.

D. Novel Contributions

The main novel contributions of this article are summarized as follows.

1) We develop an oil spill timely backtracking method oriented by deep learning-based wind field correction. The wind field correction is conducted in a spatial-temporal fashion. Benefiting from the effectiveness of the wind field correction, the proposed method achieves more accurate, timely oil spill backtracking than basic backtracking methods.
2) We develop a deep learning model, i.e., SaTCN, for the correction of historical wind fields. The SaTCN comprehensively captures both spatial correlations and temporal characteristics from the wind field sequence. It effectively produces corrected historical wind fields that approximate reanalysis wind fields. Therefore, the accurate estimate of the historical wind fields are obtained in a timely manner.
3) The proposed oil spill timely backtracking method has been validated by the experiments using data from the Sanchi and Symphony oil spill accidents. We release our codes for public evaluations at,[1] providing a baseline for oil spill timely backtracking.

E. Article Organization

The rest of this article is organized as follows. Section II describes the basic oil spill backtracking method and the proposed wind field correction-based backtracking method. Section III presents how to correct historical wind fields into more accurate ones. Section IV presents the proposed wind field correction network. Section V presents how to use the corrected historical wind fields for driving oil spill timely backtracking. Section VI presents the oil spill timely backtracking results for the Sanchi and Symphony oil spill accidents. Finally, Section VII concludes this article.

II. Oil Spill Backtracking

In this section, we describe the basic oil spill backtracking method and the proposed wind field correction-based backtracking (WFCB) method. The backtracking framework utilizes a Lagrangian oil particle model, which considers oil spills as a large concentration of particles [46]. This approach transforms oil spill backtracking into the tracking of backward migrations of particles. The backward migrations are primarily determined by two crucial factors [47], [48], i.e., historical wind fields and historical current fields. The historical current fields are highly related to the historical wind fields. The accuracy of oil spill backtracking significantly depends on the accuracy of these two fields.

The basic oil spill backtracking method is illustrated in Fig. 1(a). A present oil spill location, a historical wind field, and a historical current field are input into an oil spill backtracking

[1][Online]. Available: https://github.com/liyongqingupc/SaTCN-WindField Correction

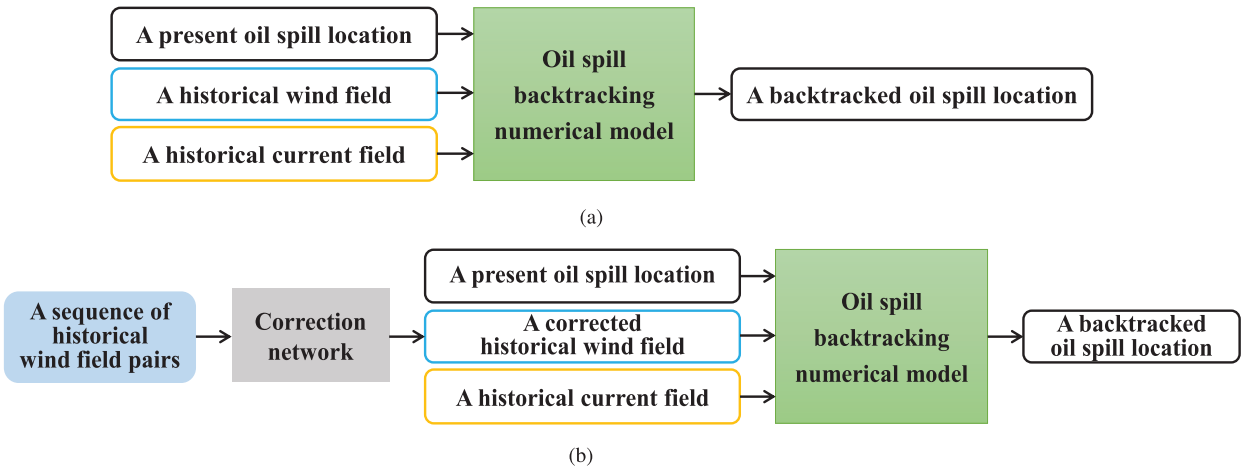

Fig. 1. Oil spill backtracking. (a) Basic oil spill backtracking. (b) Wind field correction-based oil spill backtracking.

numerical model. The model outputs a backtracked oil spill location.

The proposed WFCB method is illustrated in Fig. 1(b). The essential idea of the proposed method is to conduct oil spill timely backtracking with more accurate historical wind fields. The WFCB method utilizes the same oil spill backtracking numerical model and the historical current field as the basic oil spill backtracking method illustrated in Fig. 1(a). The main difference is that the WFCB method takes a corrected historical wind field as input instead of the historical wind field. The corrected historical wind field is obtained from the correction network that is trained with historical wind field data set.

Take a single oil particle as an example to introduce the oil spill backtracking numerical model. Let u_{b} and v_{b} denote the u (eastward) and v (northward) components of backward drift velocity for an oil particle, respectively. Let w_t^{u} and w_t^{v} denote wind velocity components at the oil particle's location at time t. They are separately obtained from the two components of the historical wind field at time t. The wind velocity in the overall direction is formulated as $w_t = ((w_t^{\mathrm{u}})^2 + (w_t^{\mathrm{v}})^2)^{1/2}$. Let c_t^{u} and c_t^{v} denote current velocity components at the oil particle's location at time t. They are separately obtained from the two components of the historical current field at time t. The two components of the oil particle backward drift velocity are formulated as follows:

$$\begin{aligned} u_{\mathrm{b}} &= \alpha_{\mathrm{w}} w_t^{\mathrm{u}} + \alpha_{\mathrm{c}} c_t^{\mathrm{u}} \\ v_{\mathrm{b}} &= \alpha_{\mathrm{w}} w_t^{\mathrm{v}} + \alpha_{\mathrm{c}} c_t^{\mathrm{v}} \end{aligned} \tag{1}$$

where α_{w} and α_{c} are balance weights for the wind velocity and the current velocity, respectively.

Let Δt denote a minimum temporal resolution for oil spill backtracking. Let Δx_{b} and Δy_{b} denote the u and v components of backward drift distance, respectively. The two distance components over a Δt interval are determined as follows:

$$\begin{aligned} \Delta x_{\mathrm{b}} &= u_{\mathrm{b}} \Delta t \\ \Delta y_{\mathrm{b}} &= v_{\mathrm{b}} \Delta t. \end{aligned} \tag{2}$$

Oil particles have a random movement process with the particle backward drift. Let R_{n} denote a random number with mean 0 and variance 1, μ denote a weighted parameter of the random movement, E_{r} denote a horizontal random movement rate, and θ denotes a directional angle that is uniformly distributed between 0 and 2π. Let Δx_{r} and Δy_{r} denote the u and v components of random movement distance, respectively. The two distance components over a Δt interval are formulated as follows:

$$\begin{aligned} \Delta x_{\mathrm{r}} &= R_{\mathrm{n}} \sqrt{\mu E_{\mathrm{r}} \Delta t} \cos\theta \\ \Delta y_{\mathrm{r}} &= R_{\mathrm{n}} \sqrt{\mu E_{\mathrm{r}} \Delta t} \sin\theta. \end{aligned} \tag{3}$$

The distance components of the oil particle backward migration are then determined as follows:

$$\begin{aligned} \Delta x &= \Delta x_{\mathrm{b}} + \Delta x_{\mathrm{r}} \\ \Delta y &= \Delta y_{\mathrm{b}} + \Delta y_{\mathrm{r}}. \end{aligned} \tag{4}$$

Let (x_t, y_t) denote the longitude and latitude coordinates of an oil particle at time t. γ is the distance corresponding to each degree of latitude at the same longitude. The backtracked coordinates $(x_{t-\Delta t}, y_{t-\Delta t})$ of the oil particle over a time interval of Δt back are formulated as follows:

$$\begin{aligned} x_{t-\Delta t} &= x_t - \Delta x/(\gamma \cos y_0) \\ y_{t-\Delta t} &= y_t - \Delta y/\gamma. \end{aligned} \tag{5}$$

The wind velocity components w_t^{u} and w_t^{v} are important factors for maintaining the performance of the oil spill backtracking. They are separately derived from the two components of the historical wind field at time t. In the early stages of an oil spill accident, only forecasted or observed wind fields are available historical wind fields. They are used for driving the basic oil spill backtracking model illustrated in Fig. 1(a). However, these wind fields are relatively inaccurate. The basic oil spill backtracking model driven by them has limited accuracy. Reanalysis wind fields are regarded as accurate historical wind field estimations but with latency of many days [49], as shown in Table I. Therefore, the reanalysis wind fields are not available in the

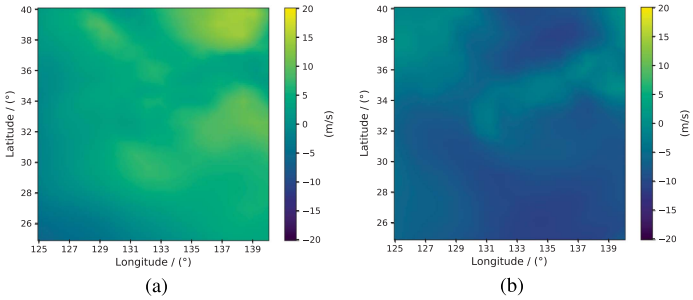

Fig. 2. Example of (a) the reanalysis wind field in the u direction and (b) the reanalysis wind field in the v direction on 1 January 2018 at 06:00 UTC.

oil spill timely backtracking. In this scenario, how to obtain accurate historical wind fields to provide accurate wind velocity components w_t^{u} and w_t^{v} for the purpose of oil spill timely backtracking is a challenging problem. As illustrated in Fig. 1(b), wind field correction provides a promising way to tackle this problem.

III. Wind Field Correction

In this section, we describe how to correct historical wind fields into more accurate ones based on deep learning. To describe the wind field correction, we first describe the wind field data used in the correction process. As introduced above, reanalysis wind fields are considered as the accurate historical wind fields. Both historical forecasted wind fields and historical observed wind fields are relatively inaccurate. To clearly describe the wind fields, we give some visual illustrations of wind field data on 1 January 2018 at 06:00 UTC. Fig. 2 illustrates the accurate reanalysis wind fields in the u and v directions separately.

Fig. 3(a) and (b) illustrates the forecasted wind field and the observed wind field in the u direction, respectively. Fig. 3(c) illustrates the histogram of wind field errors for Fig. 3(a) with respect to Fig. 2(a). Fig. 3(d) illustrates the histogram of wind field errors for Fig. 3(b) with respect to Fig. 2(a). The number in Fig. 3(c) and (d) represents the number of wind speed values in the wind field with different error levels.

Fig. 4(a) and (b) illustrates the forecasted wind field and the observed wind field in the v direction, respectively. Fig. 4(c) illustrates the histogram of wind field errors for Fig. 4(a) with respect to Fig. 2(b). Fig. 4(d) illustrates the histogram of wind field errors for Fig. 4(b) with respect to Fig. 2(b).

Fig. 5 presents the histograms of wind field errors in the overall direction.

By empirically analyzing historical wind fields in the u, v, and overall directions, we observe that the wind field errors of forecasted wind fields with respect to reanalysis wind fields are mainly in domain of $[-1, 1]$, and the wind field errors of observed wind fields with respect to reanalysis wind fields are also mainly in the domain of $[-1, 1]$. The purpose of the wind field correction is to correct historical forecasted wind fields and historical observed wind fields as close as possible to the corresponding reanalysis wind fields.

Each wind field consists of a u (eastward) component and a v (northward) component. As shown in Fig. 6, the u component and v component of each historical wind field are corrected by a u component correction network and a v component correction network, respectively. The corrections of the two components are conducted in the same way. The two correction networks have the same deep architecture but different parameter values. The input of each correction network is a sequence of historical wind field pairs where each historical wind field pair contains a forecasted wind field component and an observed wind field component. The output of each correction network is a corrected historical wind field component.

In the training phase, forecasted and observed wind field pairs in historical moments are available as inputs of the correction network, and reanalysis wind fields in the corresponding historical moments are available for correcting the outputs of the correction network. The well-trained correction network can then generate a corrected wind field given a sequence of wind field pairs. In a practical implementation when an oil spill accident has just occurred, the forecasted and observed wind fields are available but the reanalysis wind fields are not available. The correction network has the capability of correcting forecasted and observed wind fields into more accurate ones that are expected to approximate the reanalysis wind fields. It thus provides more accurate historical wind fields than the forecasted wind fields and the observed wind fields in the historical moments. Therefore, the WFCB method illustrated in Fig. 1(b) can give backtracked oil spill coordinates with higher accuracy than the basic backtracking method illustrated in Fig. 1(a).

Wind field correction is the process of correcting the forecasted and observed historical wind fields into more accurate historical wind fields. How to design a deep architecture for the correction network for the purpose of rendering accurate correction of the inaccurate historical wind fields (i.e., the forecasted and observed wind fields) is a challenging problem.

IV. Self-Attention Temporal Convolutional Networks

In this section, we introduce a deep architecture, i.e., SaTCN, for the wind field correction network. Section IV-A describes the main architecture of the SaTCN framework, which consists of a self-attention network and a temporal convolutional network. Section IV-B describes the architecture of the self-attention network. Section IV-C describes the architecture of the temporal convolutional network. Section IV-D describes the training procedure of the SaTCN framework.

A. Main Architecture

The SaTCN framework corrects historical wind fields. The main architecture of the SaTCN framework is illustrated in Fig. 7. Take one wind field component (u or v) as an example, and the component is of $M \times N$ size. Let $\boldsymbol{W}_t^{\mathrm{f}} \in \mathbb{R}^{M\times N}$ and $\boldsymbol{W}_t^{\mathrm{o}} \in \mathbb{R}^{M\times N}$ denote a forecasted wind field component and an observed wind field component at time t, respectively. As

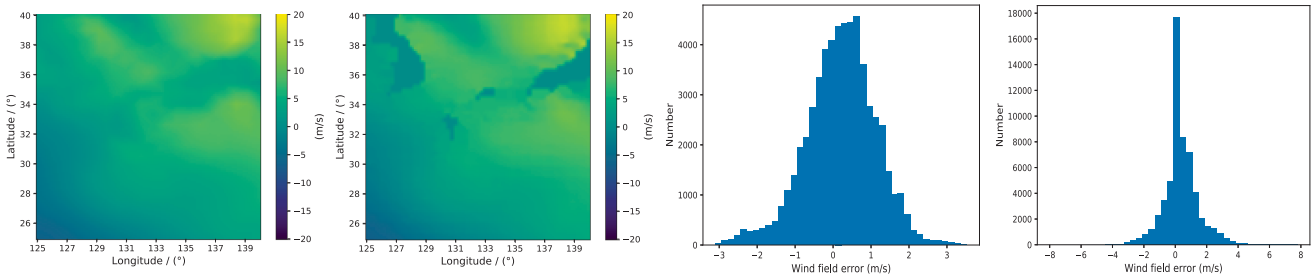

Fig. 3. Example of (a) the forecasted wind field, (b) the observed wind field, (c) the histogram of errors for the forecasted wind field with respect to the reanalysis wind field, and (d) the histogram of errors for the observed wind field with respect to the reanalysis wind field on 1 January 2018 at 06:00 UTC in the u direction.

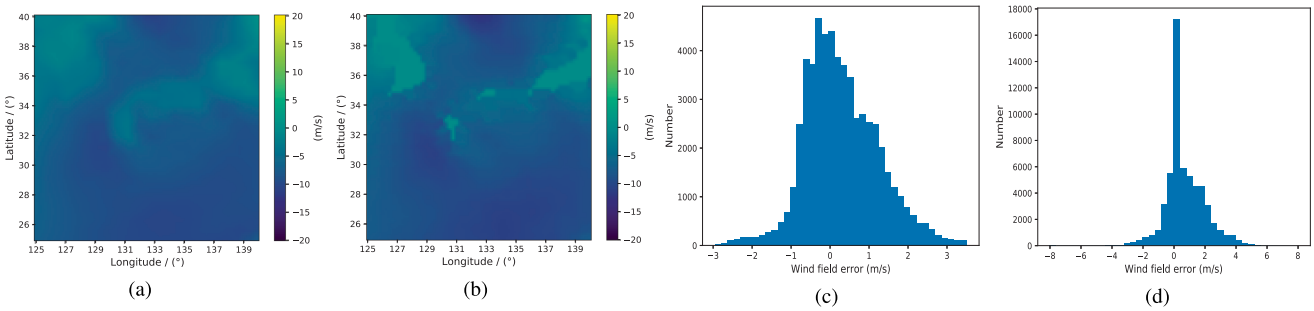

Fig. 4. Example of (a) the forecasted wind field, (b) the observed wind field, (c) the histogram of errors for the forecasted wind field with respect to the reanalysis wind field, and (d) the histogram of errors for the observed wind field with respect to the reanalysis wind field on 1 January 2018 at 06:00 UTC in the v direction.

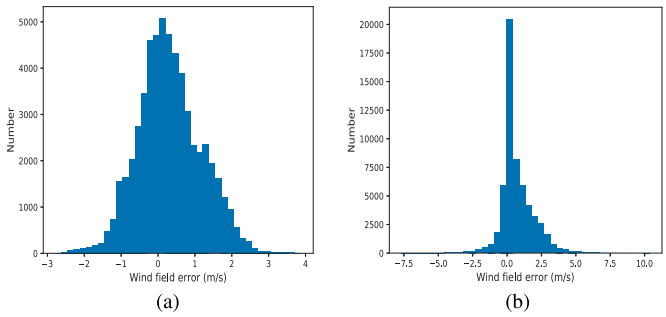

Fig. 5. Histogram of (a) errors for the forecasted wind field with respect to the reanalysis wind field and (b) errors for the observed wind field with respect to the reanalysis wind field on 1 January 2018 at 06:00 UTC in the overall direction.

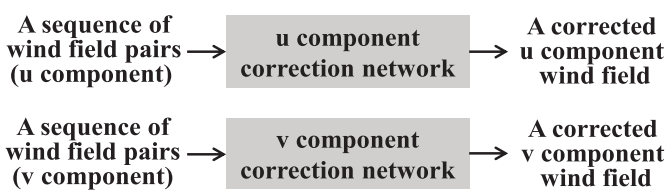

Fig. 6. Wind field component correction.

shown in Fig. 8, $\mathcal{W}_t = [\boldsymbol{W}_t^{\mathrm{f}}, \boldsymbol{W}_t^{\mathrm{o}}] \in \mathbb{R}^{2\times M\times N}$ denotes a historical wind field pair at time t. The corrected historical wind field component denoted as $\boldsymbol{W}_t^{\mathrm{c}}$ and the reanalysis wind field component denoted as $\boldsymbol{W}_t^{\mathrm{r}}$ have the same dimension as $\boldsymbol{W}_t^{\mathrm{f}}$.

The SaTCN takes a sequence of historical wind field pairs $\{\mathcal{W}_{t-T_1}, \ldots, \mathcal{W}_t, \ldots, \mathcal{W}_{t+T_2}\}$ as input, extracts spatial and temporal characteristics from them, and outputs a corrected historical wind field component $\boldsymbol{W}_t^{\mathrm{c}}$ for $\mathcal{W}_t$. The SaTCN consists of a self-attention network and a temporal convolutional network. The self-attention network contains $(T_1 + T_2 + 1)$ self-attention modules whose number is governed by the length of the historical wind field sequence. The temporal convolutional network is constructed by cascaded 3DCNN modules and 2-D convolutional neural network (2DCNN) modules.

The self-attention network captures the global spatial correlations of a historical wind field pair sequence. The temporal convolutional network captures the local spatial correlations and the temporal characteristics of an attention weighted wind field sequence. These network properties enhance the SaTCN's representational power and facilitate the SaTCN to output more accurate corrected historical wind fields.

B. *Self-Attention Network*

The self-attention network consists of $(T_1 + T_2 + 1)$ self-attention modules. The self-attention network takes a sequence of historical wind field pairs $\{\mathcal{W}_{t-T_1}, \ldots, \mathcal{W}_t, \ldots, \mathcal{W}_{t+T_2}\}$ as input and outputs an attention weighted wind field sequence $\{\mathcal{S}_{t-T_1}, \ldots, \mathcal{S}_t, \ldots, \mathcal{S}_{t+T_2}\}$. The main architecture of the self-attention module at time t is illustrated in Fig. 9. The self-attention module takes $\mathcal{W}_t$ as input and outputs an attention weighted wind field $\mathcal{S}_t$.

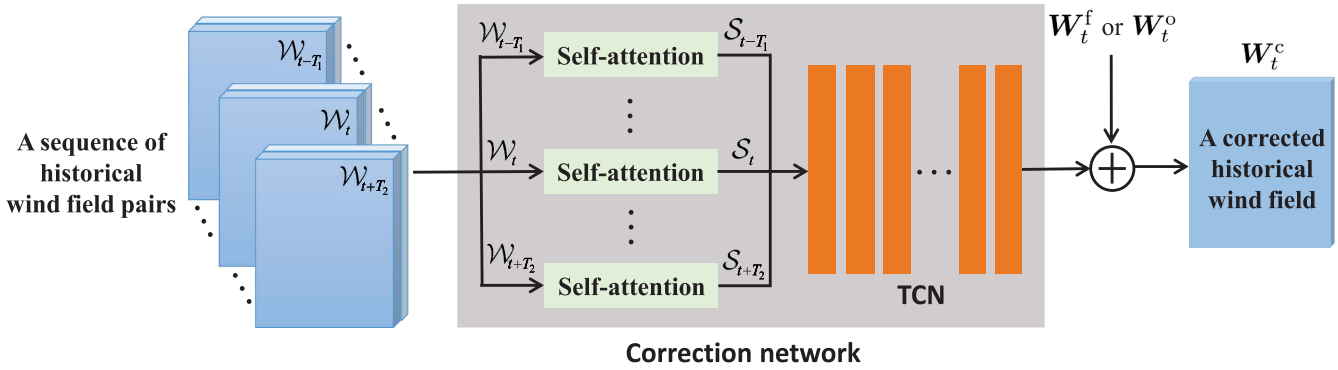

Fig. 7. SaTCN for historical wind field correction.

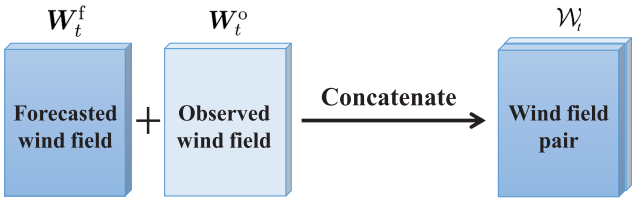

Fig. 8. Wind field pair at time t.

As shown in Fig. 9, $\mathcal{W}_t \in \mathbb{R}^{2\times M\times N}$ is assigned three 1×1 convolutional operations to obtain three feature maps containing query $\boldsymbol{Q}\in\mathbb{R}^{M\times N}$, key $\boldsymbol{K}\in\mathbb{R}^{M\times N}$, and value $\boldsymbol{V}\in\mathbb{R}^{2\times M\times N}$. Let $\boldsymbol{Q}_{\mathrm{r}}\in\mathbb{R}^{1\times MN}$, $\boldsymbol{K}_{\mathrm{r}}\in\mathbb{R}^{1\times MN}$, and $\boldsymbol{V}_{\mathrm{r}}\in\mathbb{R}^{2\times MN}$ denote the variables reshaped from $\boldsymbol{Q}$, $\boldsymbol{K}$, and $\boldsymbol{V}$, respectively. The self-attention weight matrix $\omega\in\mathbb{R}^{MN\times MN}$ is computed as follows [50]:

$$\omega=\mathrm{softmax}(\boldsymbol{Q}_{\mathrm{r}}^{\mathrm{T}}\boldsymbol{K}_{\mathrm{r}}) \tag{6}$$

where $\mathrm{softmax}(\cdot)$ denotes the softmax operation.

The attention feature map $\mathcal{A}\in\mathbb{R}^{2\times M\times N}$ is computed as follows:

$$\mathcal{A}=\mathrm{Reshape}(\boldsymbol{V}_{\mathrm{r}}\omega^{\mathrm{T}}) \tag{7}$$

where $\mathrm{Reshape}(\cdot)$ denotes the reshape operation $2\times MN\rightarrow 2\times M\times N$.

The output of the self-attention module is an attention weighted wind field $\mathcal{S}_t\in\mathbb{R}^{2\times M\times N}$ that is computed as follows [51]:

$$\mathcal{S}_t=\mathrm{Conv}(\mathcal{A})+\mathcal{W}_t \tag{8}$$

where $\mathrm{Conv}(\cdot)$ denotes the 1×1 convolutional operation.

The self-attention module establishes connections for all wind velocities in the wind field pair $\mathcal{W}_t$ by computing the self-attention weight matrix ω. It facilitates to capture the global spatial correlations for each historical wind field pair.

C. Temporal Convolutional Network

The main architecture of the temporal convolutional network (TCN) is illustrated in Fig. 10. In our research, the TCN part of the SaTCN is constructed by L cascaded 3DCNN modules and one 2DCNN module. The TCN takes a sequence of attention weighted wind fields $\{\mathcal{S}_{t-T_1},\ldots,\mathcal{S}_t,\ldots,\mathcal{S}_{t+T_2}\}$ as input and outputs a wind field correction residual $\boldsymbol{W}_t{}'$.

The 3DCNN modules are conducted with causal convolution operations. Let $\{\mathcal{H}^l_{t-T_1},\ldots,\mathcal{H}^l_t,\ldots,\mathcal{H}^l_{t+T_2}\}$ denote a feature map sequence output by lth 3DCNN module, where $1\le l\le L$. It is computed as follows:

$$\begin{aligned}&\{\mathcal{H}^l_{t-T_1},\ldots,\mathcal{H}^l_t,\ldots,\mathcal{H}^l_{t+T_2}\}\\&\quad=\mathrm{3DCNN}(\mathcal{Z},\mathcal{H}^{l-1}_{t-T_1},\ldots,\mathcal{H}^{l-1}_t,\ldots,\mathcal{H}^{l-1}_{t+T_2})\end{aligned} \tag{9}$$

where $\mathrm{3DCNN}(\cdot)$ represents the function of 3DCNN module [52] and $\mathcal{Z}\in\mathbb{R}^{2\times M\times N}$ is a zero tensor for padding operation. The causal convolution implies that the $\mathcal{H}^l_t$ is only determined by the feature map sequence $\{\mathcal{Z},\mathcal{H}^{l-1}_{t-T_1},\ldots,\mathcal{H}^{l-1}_t\}$. The L th 3DCNN module outputs $\{\mathcal{H}^L_{t-T_1},\ldots,\mathcal{H}^L_t,\ldots,\mathcal{H}^L_{t+T_2}\}$. The subsequent 2DCNN module takes them as input and outputs $\boldsymbol{W}_t{}'$ as follows:

$$\boldsymbol{W}_t{}'=\mathrm{2DCNN}\left(\mathcal{H}^L_{t-T_1},\ldots,\mathcal{H}^L_t,\ldots,\mathcal{H}^L_{t+T_2}\right) \tag{10}$$

where $\mathrm{2DCNN}(\cdot)$ represents the function of 2DCNN module.

As illustrated in Fig. 7, the SaTCN utilizes residual learning mechanism to learn the differences between the historical wind field ($\boldsymbol{W}^{\mathrm{f}}_t$ or $\boldsymbol{W}^{\mathrm{o}}_t$) and the reanalysis wind field $\boldsymbol{W}^{\mathrm{r}}_t$. The historical wind field is adopted by the principle of having higher spatial resolution. The corrected historical wind field $\boldsymbol{W}^{\mathrm{c}}_t$ is formulated as follows:

$$\boldsymbol{W}^{\mathrm{c}}_t=\begin{cases}\boldsymbol{W}^{\mathrm{f}}_t+\boldsymbol{W}_t{}' & \text{for } \boldsymbol{W}^{\mathrm{f}}_t \text{ has high resolution}\\ \boldsymbol{W}^{\mathrm{o}}_t+\boldsymbol{W}_t{}' & \text{for } \boldsymbol{W}^{\mathrm{o}}_t \text{ has high resolution.}\end{cases} \tag{11}$$

The SaTCN framework plays a key role in extracting spatial and temporal characteristics from the input wind field pair sequence. Specifically, the self-attention part of the SaTCN extracts the global spatial correlations and the TCN part of the SaTCN extracts the temporal characteristics and the local spatial correlations. These extracted spatial-temporal characteristics are integrated by the 2DCNN module to produce the accurate corrected historical wind field $\boldsymbol{W}^{\mathrm{c}}_t$.

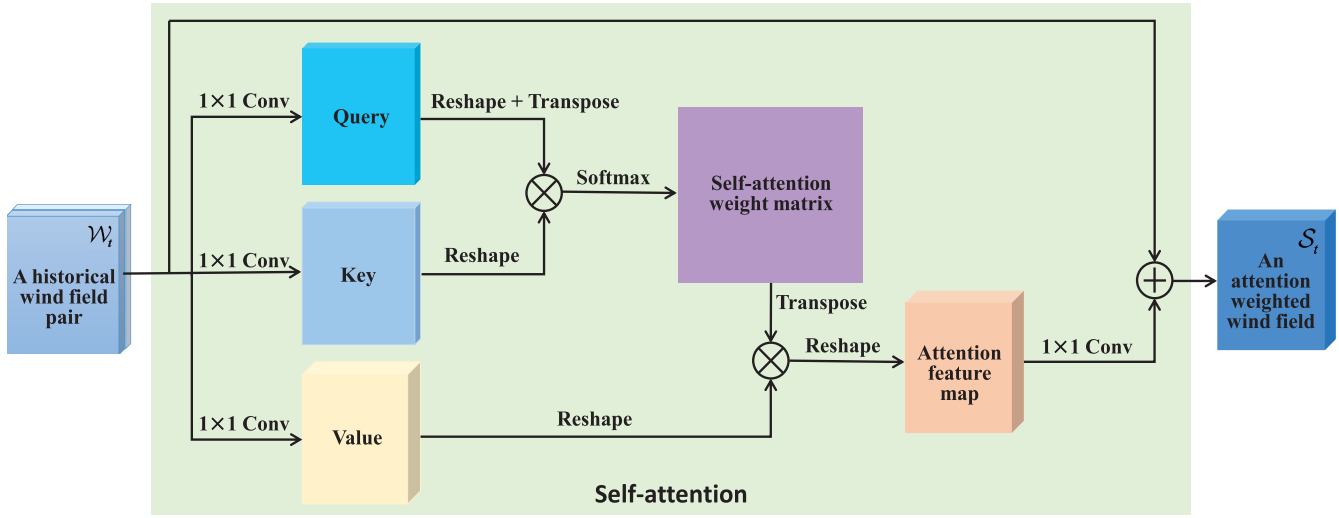

Fig. 9. Self-attention module.

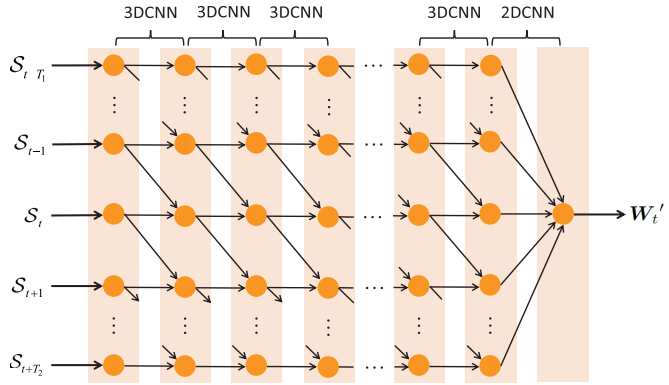

Fig. 10. Temporal convolutional network.

D. Training the SaTCN

The SaTCN is trained with historical wind field data. The training loss L_{S} for the SaTCN is given as follows:

$$L_{\mathrm{S}} = \left\| \boldsymbol{W}_t^{\mathrm{r}} - \boldsymbol{W}_t^{\mathrm{c}} \right\|_1 \tag{12}$$

where L_{S} is called ℓ_1 norm loss. Minimizing (12) trains the SaTCN to generate $\boldsymbol{W}_t^{\mathrm{c}}$ as close to $\boldsymbol{W}_t^{\mathrm{r}}$ as possible.

The training procedure of the SaTCN is described in Algorithm 1. The SaTCN is trained in cycles such that its correction ability is gradually improved. The training terminates when the SaTCN achieves optimal correction accuracies. Finally, the well-trained SaTCN is capable of producing accurate corrected historical wind fields.

Algorithm 1: Training Procedure of the SaTCN Framework.

Input: The training set consisting of forecasted wind fields, observed wind fields, and their corresponding reanalysis wind fields
Output: The trained parameter set of the SaTCN
for all training epochs **do**
  for all training samples **do**
    Input a historical wind field pair sequence $\{\mathcal{W}_{t-T_1}, \ldots, \mathcal{W}_t, \ldots, \mathcal{W}_{t+T_2}\}$ and a reanalysis wind field $\boldsymbol{W}_t^{\mathrm{r}}$;
    Compute $\boldsymbol{W}_t^{\mathrm{c}}$ according to (11);
    Compute L_{S} according to (12) and update the parameters of the SaTCN.
  end for
end for

V. Oil Spill Timely Backtracking Driven by Corrected Historical Wind Fields

In this section, we present the procedure of historical wind field correction via the SaTCN and the procedure of using the corrected historical wind fields for driving oil spill timely backtracking. After the training described in Section IV-D, a well-trained SaTCN is ready for applications. In practical operations, the SaTCN takes a sequence of historical wind field pairs as input and outputs a corrected historical wind field $\boldsymbol{W}_t^{\mathrm{c}}$ for the specific wind field pair at time t. The corrected historical wind field $\boldsymbol{W}_t^{\mathrm{c}}$ is utilized to provide the wind velocity components w_t^{u} or w_t^{v} in (1). It provides accurate historical wind velocity components for oil spill timely backtracking. The backtracked oil spill coordinates are obtained according to (1)–(5).

Though the SaTCN requires reanalysis wind fields for training, it does not require them in the practical operations. The SaTCN can correct historical wind fields in a timely manner. The corrected historical wind fields do not suffer from the time latency associated with the reanalysis wind fields but approximate the accuracy of the reanalysis wind fields. Therefore, the corrected historical wind fields enable timely, accurate oil spill backtracking.

VI. Experimental Results

In this section, we conduct extensive backtracking experiments on Sanchi and Symphony oil spill accidents to evaluate the effectiveness of the proposed backtracking method oriented by the wind field correction with the SaTCN.

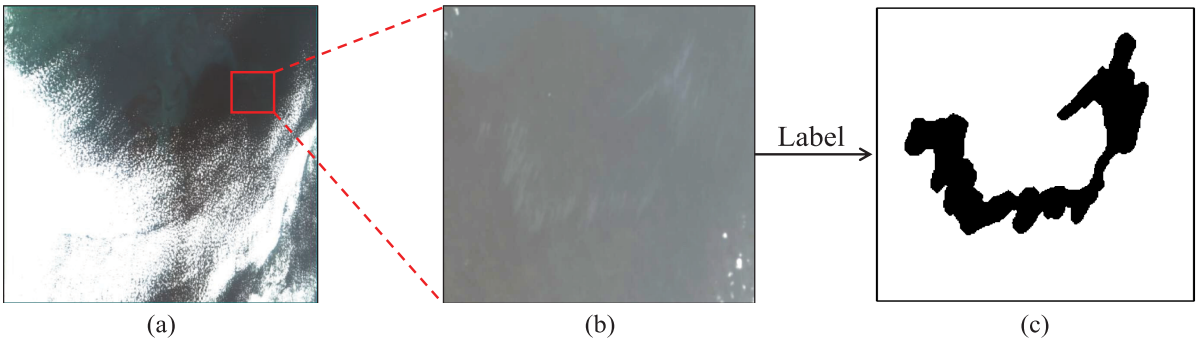

Fig. 11. Sanchi oil spill observation image and its oil spill labeling. (a) Remote sensing image captured by GF-1 satellite on January 20, 2018 at 11:17 UTC. (b) Image patch containing Sanchi oil spills. (c) Detected oil spill locations in (b).

TABLE II
WIND FIELD DATA USED FOR SANCHI OIL SPILL BACKTRACKING

Wind type	Data source	Spatial resolution	Temporal resolution
Forecasted	ECMWF	$0.125° \times 0.125°$	6 h
Observed	CMEMS	$0.25° \times 0.25°$	6 h
Reanalysis	ECMWF	$0.125° \times 0.125°$	6 h

TABLE III
DETAILED INFORMATION OF THE REMOTE SENSING IMAGES USED IN THE EXPERIMENTS

File name	Satellite	Capture time	Size
GF1_WFV4_E125.4_N28.4_20180120_ L1A0002945335.tiff	GF-1	2018-01-20 11:17	13400 × 12000
S1A_IW_GRDH_1SDV_20210501T095610_ 20210501T095635_037693_047292_191D	Sentinel-1	2021-05-01 09:56	16718 × 25527

A. Experimental Settings and Evaluation Metrics

In this subsection, we describe experimental settings and evaluation metrics used in the experiments. The numerical backtracking model is implemented with PyCharm on a PC platform. Based on empirical evaluations, the wind velocity weight α_w is set to 0.03 and the current velocity weight α_c is set to 1. The SaTCN model is implemented with Tensorflow 1.15.0 framework. A platform with 2 Intel Xeon Gold 5218R CPUs and 2 NVIDIA Geforce 2080Ti GPUs are used to deploy the experimental environment.

1) Experimental Settings for Sanchi Oil Spill Backtracking: The Sanchi oil spill accident happened about 160 nautical miles east of the Yangtze River estuary on January 6, 2018 at about 12:00 UTC. The oil tanker Sanchi caught fire after the collision and sank on January 14, 2018 at 08:45 UTC, which is set as the end time of the oil spill backtracking. The sinking site was located at (28°22′N, 125°55′E) where a large amounts of condensate oil and fuel oil began to leak on the sea surface.

As shown in Fig. 11(a), the Sanchi oil spill remote sensing image used in the experiments was captured by GF-1 satellite on January 20, 2018 at 11:17 UTC, which is set as the starting time of the oil spill backtracking. Fig. 11(b) is the image patch containing Sanchi oil spills. The oil spill locations in the remote sensing image are labeled manually. Fig. 11(c) is the detected oil spill locations in Fig. 11(b). The detection method is implemented based on open-source code.[2] The detailed information of the remote sensing images used in the experiments is described in Table III.

To train and test the wind field correction networks for Sanchi oil spill timely backtracking, we build a wind field data set containing forecasted wind fields, observed wind fields, and reanalysis wind fields. The forecasted and reanalysis wind fields are obtained from an ERA-Interim archive of ECMWF.[3] The ERA-Interim is a part of ECMWF's meteorological archive and retrieval system. The ERA-Interim provides coupled forecasted and reanalysis wind fields at the same time. The reanalysis wind fields provide a benchmark for the historical wind field correction. The observed wind fields are obtained from CMEMS.[4] The detailed wind field information used for Sanchi oil spill backtracking is described in Table II.

To investigate the historical wind field correction for the Sanchi oil spill backtracking, we use the wind field data of

[2][Online]. Available: https://github.com/liyongqingupc/MCAN-OilSpillDetection

[3][Online]. Available: https://apps.ecmwf.int/datasets/data/interim-full-daily/levtype=sfc/

[4][Online]. Available: https://resources.marine.copernicus.eu/product-detail/WIND_GLO_WIND_L4_REP_OBSERVATIONS_012_006/INFORMATION

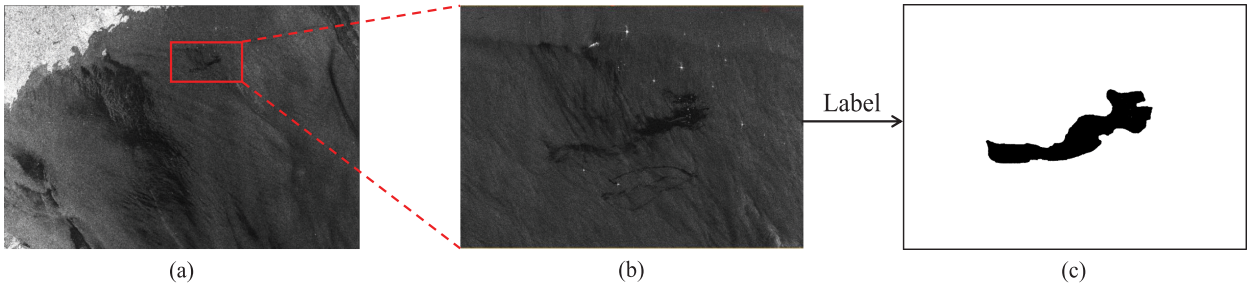

Fig. 12. Symphony oil spill observation image and its oil spill labeling. (a) Remote sensing image captured by Sentinel-1 satellite on May 1st, 2021 at 09:56 UTC. (b) Image patch containing Symphony oil spills. (c) Detected oil spill locations in (b).

a square area with upper left located at $(40°\mathrm{N}, 125°\mathrm{E})$ and lower right located at $(25°\mathrm{N}, 140°\mathrm{E})$. To guarantee the precision of the oil spill backtracking, we set the spatial resolution as $0.125° \times 0.125°$ and set the temporal resolution as 6 h. The observed wind fields meet the spatial resolution requirement by interpolation operations. Each wind field data have two components with a size of $2 \times 121 \times 121$. The time range of the wind field data set is from January 1, 2018 to June 30, 2018. For each wind field type, there are 724 wind field data used to conduct experiments, where the 600 data ranging from February to June are used to train the correction models and the 124 data of January to test the correction performances.

The historical current fields used in backtracking model are downloaded from the HYCOM data set GLBv0.08/expt_93.0.[5] The spatial resolution of the historical current fields is $0.08° \times 0.08°$ and the temporal resolution of that is 6 h.

2) Experimental Settings for Symphony Oil Spill Backtracking: The Symphony oil spill accident happened in the south of the Qingdao port on April 27, 2021 at 00:51 UTC, which is set as the end time of the oil spill backtracking. The Liberian oil tanker Symphony was smashed by the Panamanian cargo ship Sea Justice. A large amounts of oil leaked on the sea surface. The accident was located at $(35°43'\mathrm{N}, 120°58'\mathrm{E})$.

As shown in Fig. 12(a), the Symphony oil spill remote sensing image used in the experiments was captured by Sentinel-1 satellite on May 1, 2021 at 09:56 UTC, which is set as the starting time of the oil spill backtracking. Fig. 12(b) is the image patch containing Symphony oil spills. The oil spill locations in the remote sensing image are labeled manually. Fig. 12(c) is the detected oil spill locations in Fig. 12(b). The detailed information of the remote sensing images used in the experiments is described in Table III.

To train and test the wind field correction networks for the Symphony oil spill backtracking, we build a wind field data set containing forecasted wind fields, observed wind fields, and reanalysis wind fields. The forecasted wind fields are obtained from NCEP-GFS archive.[6] The reanalysis wind fields are obtained from an ERA5 archive of ECMWF,[7] and they provide a benchmark for the historical wind field correction. The observed wind fields are obtained from CMEMS.[8] The detailed wind field information used for Symphony oil spill backtracking is described in Table IV.

To investigate the historical wind field correction for the Symphony oil spill backtracking, we use the wind field data of a square area with upper left located at $(40°\mathrm{N}, 110°\mathrm{E})$ and lower right located at $(25°\mathrm{N}, 125°\mathrm{E})$. To guarantee the precision of the backtracking, we set the spatial resolution as $0.125° \times 0.125°$ and set the temporal resolution as 6 h. The forecasted and reanalysis wind fields meet the spatial resolution requirement by interpolation operations. The time range of the wind field data set is from April 1, 2021 to September 30, 2021. For each wind field type, there are 732 wind field data used to conduct experiments, where the 124 data ranging from April 1 to May 1 to test the correction performances and the rest 608 wind field data are used to train the correction models.

The historical current fields used in backtracking model are downloaded from the HYCOM data set GLBy0.08/expt_93.0.[9] The spatial resolution of the historical current fields is $0.08° \times 0.08°$ and the temporal resolution of that is 3 h.

3) Experimental Settings for Wind Field Correction: To validate the effectiveness of the proposed SaTCN framework, we compare the correction performance of the SaTCN with those of ConvLSTM [43], hierarchical generative adversarial network (HGAN) [53], and temporal convolutional network (TCN) [45]. The ConvLSTM network is implemented based on open-source code.[10] The HGAN is implemented based on open-source code.[11] The TCN is an improved version based on open-source code.[12]

The parameters for training the SaTCN in the experiments are set as follows. The number of the 3DCNN modules is set as $L = 4$. The input sequence length $(T_1 + T_2 + 1)$ is set to 4, where $T_1 = 2$ and $T_2 = 1$. The learning rate is set to 0.0005. The SaTCN is trained with an Adam optimizer. The parameter configuration for the SaTCN framework is presented in Table V.

4) Experimental Evaluation Metrics: Let (x_s, y_s) denote the longitude and latitude coordinates of the true oil spill source.

[5][Online]. Available: http://tds.hycom.org/thredds/catalogs/GLBv0.08/expt_93.0.html?dataset=GLBv0.08-expt_93.0

[6][Online]. Available: https://rda.ucar.edu/datasets/ds084.1/#!access

[7][Online]. Available: https://cds.climate.copernicus.eu/cdsapp#!/dataset/reanalysis-era5-single-levels?tab=form

[8][Online]. Available: https://resources.marine.copernicus.eu/product-detail/WIND_GLO_PHY_L4_NRT_012_004/INFORMATION

[9][Online]. Available: http://tds.hycom.org/thredds/catalogs/GLBy0.08/expt_93.0.html?dataset=GLBy0.08-expt_93.0

[10][Online]. Available: https://github.com/giserh/ConvLSTM-2

[11][Online]. Available: https://github.com/lihuiupc/HGAN-TyphoonCloudVisualPrediction

[12][Online]. Available: https://github.com/philipperemy/keras-tcn

TABLE IV
WIND FIELD DATA USED FOR SYMPHONY OIL SPILL BACKTRACKING

Wind type	Data source	Spatial resolution	Temporal resolution
Forecasted	NCEP-GFS	$0.25° \times 0.25°$	6 h
Observed	CMEMS	$0.125° \times 0.125°$	1 h
Reanalysis	ECMWF	$0.25° \times 0.25°$	1 h

TABLE V
PARAMETER CONFIGURATION FOR THE SATCN FRAMEWORK

Net	Layer	Filter	Kernel	Padding
Sa	2DCNN ($\boldsymbol{Q}$)	1	1×1	same
	2DCNN ($\boldsymbol{K}$)	1	1×1	same
	2DCNN ($\boldsymbol{V}$)	2	1×1	same
	2DCNN ($\mathcal{A}$)	2	1×1	same
TCN	3DCNN + LReLU	256	3×3	causal
	3DCNN + LReLU	128	3×3	causal
	3DCNN + LReLU	64	3×3	causal
	3DCNN + LReLU	32	3×3	causal
	2DCNN	1	1×1	same

Let $(x_{\mathrm{b}}, y_{\mathrm{b}})$ denote the longitude and latitude coordinates of the backtracked oil spill source. Let $(x_{\mathrm{e}}, y_{\mathrm{e}})$ denote the coordinate errors of backtracking. $(x_{\mathrm{e}}, y_{\mathrm{e}})$ is formulated as follows:

$$(x_{\mathrm{e}}, y_{\mathrm{e}}) = |(x_{\mathrm{s}}, y_{\mathrm{s}}) - (x_{\mathrm{b}}, y_{\mathrm{b}})|. \tag{13}$$

Let R denote the radius of the earth. The distance error of backtracking is formulated as follows:

$$E_{\mathrm{d}} = R \arccos[\cos(y_{\mathrm{s}}) \cos(y_{\mathrm{b}}) \cos(x_{\mathrm{s}} - x_{\mathrm{b}}) + \sin(y_{\mathrm{s}}) \sin(y_{\mathrm{b}})] \pi / 180. \tag{14}$$

To evaluate historical wind field correction performances of different deep learning models, we utilize some quantitative evaluation criteria to demonstrate the effectiveness of the proposed model. Let $\boldsymbol{W}_t^{\mathrm{c}}$ and $\boldsymbol{W}_t^{\mathrm{r}}$ denote a corrected historical wind field component (either u or v) and a corresponding reanalysis wind field component.

Root-mean-squared error (rmse) is usually used as an evaluation criterion of errors and it is formulated as follows:

$$\mathrm{RMSE} = \sqrt{\frac{1}{MN} \sum_{m=1}^{M} \sum_{n=1}^{N} [\boldsymbol{W}_t^{\mathrm{c}}(m,n) - \boldsymbol{W}_t^{\mathrm{r}}(m,n)]^2} \tag{15}$$

where M and N denote the height (rows) and width (columns) of a wind field component, respectively.

Mean absolute error (MAE) is an average value of the absolute errors between two wind field components and it is formulated as follows:

$$\mathrm{MAE} = \frac{1}{MN} \sum_{m=1}^{M} \sum_{n=1}^{N} |\boldsymbol{W}_t^{\mathrm{c}}(m,n) - \boldsymbol{W}_t^{\mathrm{r}}(m,n)|. \tag{16}$$

RMSE and MAE are used to quantitatively evaluate the historical wind field correction performances in Section VI-B.

B. Comparisons With Different Deep Learning Methods

In this subsection, we evaluate the effectiveness of the proposed SaTCN framework by comparing it with three different deep learning networks (ConvLSTM [43], HGAN [53], and TCN [45]). Forecasted and observed wind fields provide baselines for comparing the correction performances of four deep learning networks. The ConvLSTM, HGAN, and TCN are separately trained and tested with the same data sets, learning rate, and optimizer as the SaTCN.

As shown in Fig. 13, the correction performances of four deep learning networks are compared subject to RMSE and MAE between January 14, 2018 at 00:00 UTC and January 20, 2018 at 18:00 UTC. The lower the curve, the better the correction performance. Two evaluation results [see Fig. 13(a) and (b)] of the four networks are all below the red lines. It is demonstrated that the four networks have achieved different degrees of wind field correction. The correction performance of the SaTCN outperforms the other three networks.

Table VI presents the average correction results for historical wind fields in u, v, and overall directions between January 14, 2018 at 00:00 UTC and January 20, 2018 at 18:00 UTC. It is quantitatively validated that the correction errors of the SaTCN are all less than those of the other three methods in three cases.

As shown in Fig. 14, the correction performances of the four networks are compared subject to rmse and MAE between April 27, 2021 at 00:00 UTC and May 1, 2021 at 18:00 UTC. Two evaluation results [see Fig. 14(a) and (b)] of the four networks

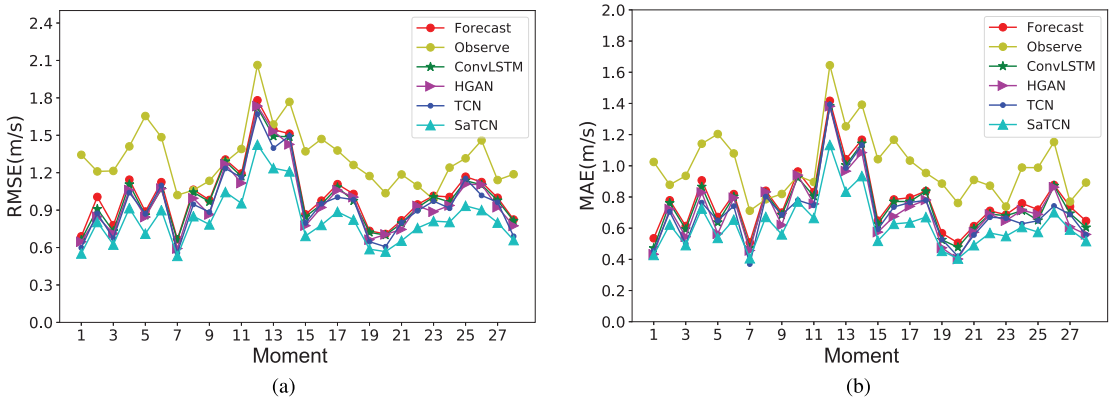

Fig. 13. Correction performance comparison based on rmse and MAE of four methods between January 14, 2018 at 00:00 UTC and January 20, 2018 at 18:00 UTC. (a) RMSE of four correction methods at 28 moments with 6 h intervals. (b) MAE of four correction methods at 28 moments with 6 h intervals.

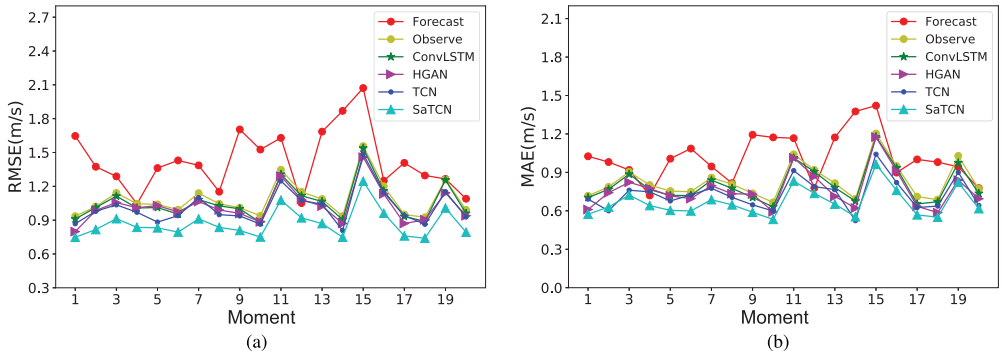

Fig. 14. Correction performance comparison based on rmse and MAE of four methods between April 27, 2021 at 00:00 UTC and May 1, 2021 at 18:00 UTC. (a) RMSE of four correction methods at 20 moments with 6 h intervals. (b) MAE of four correction methods at 20 moments with 6 h intervals.

are all below the orange lines. The correction performance of the SaTCN outperforms the other three networks.

Table VII presents the average correction results for historical wind fields in u, v, and overall directions between April 27, 2021 at 00:00 UTC and May 1, 2021 at 18:00 UTC. It is quantitatively validated that the correction errors of the SaTCN are all less than those of the other three methods in three cases.

Table VIII presents the average correction results on two test sets in the overall direction. Compared with forecasted wind fields, the SaTCN achieves an average 14.14% reduction in rmse and an average 9.71% reduction in MAE on the test set for the Sanchi oil spill backtracking. Compared with observed wind fields, the SaTCN achieves an average 11.63% reduction in rmse and an average 16.45% reduction in MAE on the test set for the Symphony oil spill backtracking. To evaluate the effectiveness of the wind field pairs in the historical wind field correction, we train the four deep learning models with two different inputs separately.

As shown in Table VIII, the correction performances of the four models are compared in terms of double inputs and single input. The term of double inputs implies that the models take a sequence of forecasted and observed wind field pairs as input. For Sanchi oil spill backtracking, the term of single input implies that the models take a sequence of forecasted wind field components as input. For Symphony oil spill backtracking, the single input implies that the models take a sequence of observed wind field components as input. It is obviously shown that all networks trained with double inputs have better correction performances than those with single input. Therefore, with regard to two evaluation criteria, the overall correction performance of our proposed SaTCN outperforms the other three deep learning models.

C. Sanchi Oil Spill Backtracking

In this subsection, we validate the effectiveness of the wind field correction-based backtracking (WFCB) method on the Sanchi oil spill accident. In this experiment, we assume that the oil spill backtracking started from the time when the remote sensing image [shown in Fig. 11(a)] had been just acquired. At that time, if the operation of oil spill backtracking was required to be conducted immediately, the only available data for wind fields were the relatively inaccurate forecasted wind fields and observed wind fields. Meanwhile, the reanalysis wind fields were not available. In this scenario, the timely, accurate oil spill backtracking should be conducted based on the corrected historical wind fields from the relatively inaccurate forecasted wind fields and observed wind fields.

Section VI-B has demonstrated that the proposed SaTCN has a better correction performance between January 1, 2018 at 00:00 UTC and January 31, 2018 at 18:00 UTC. The corrected historical wind fields are more similar to the reanalysis wind

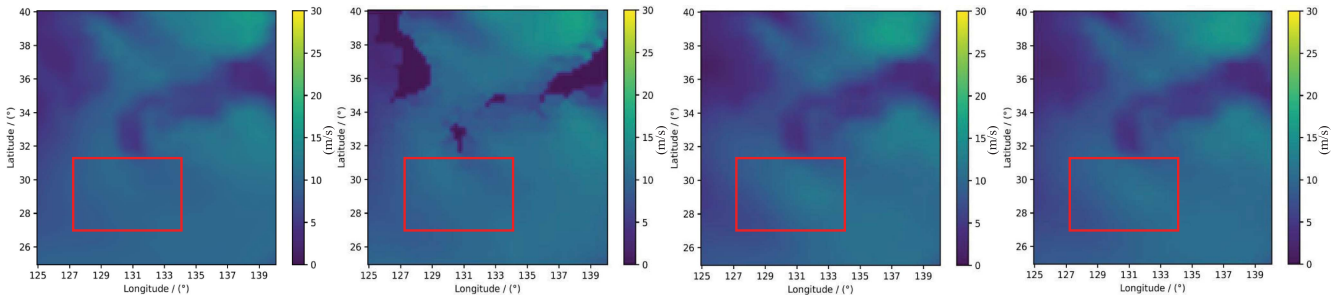

Fig. 15. Visual illustrations of (a) the forecasted wind field, (b) the observed wind field, (c) the reanalysis wind field, and (d) the corrected historical wind field from the SaTCN on January 1, 2018 at 06:00 UTC in the overall direction.

TABLE VI
AVERAGE CORRECTION RESULTS FOR HISTORICAL WIND FIELDS IN U, V, AND OVERALL DIRECTIONS BETWEEN JANUARY 14, 2018 AT 00:00 UTC AND JANUARY 20, 2018 AT 18:00 UTC

Direction	Method	RMSE	MAE
u	Forecasted	1.1167	0.8440
	Observed	1.3070	0.9836
	ConvLSTM	1.0243	0.8234
	HGAN	0.9876	0.7988
	TCN	0.9264	0.7854
	SaTCN	**0.8845**	**0.7234**
v	Forecasted	1.1130	0.8389
	Observed	1.3542	1.0239
	ConvLSTM	1.0842	0.8145
	HGAN	1.0134	0.8021
	TCN	0.9986	0.7985
	SaTCN	**0.9256**	**0.7562**
Overall	Forecasted	1.0358	0.7744
	Observed	1.3187	0.9949
	ConvLSTM	1.0011	0.7567
	HGAN	0.9879	0.7482
	TCN	0.9457	0.7234
	SaTCN	**0.9354**	**0.7052**

The bold values represent the smallest error values.

TABLE VII
AVERAGE CORRECTION RESULTS FOR HISTORICAL WIND FIELDS IN U, V, AND OVERALL DIRECTIONS BETWEEN APRIL 27, 2021 AT 00:00 UTC AND MAY 1, 2021 AT 18:00 UTC

Direction	Method	RMSE	MAE
u	Forecasted	1.4226	1.0015
	Observed	1.0401	0.7727
	ConvLSTM	1.0354	0.7234
	HGAN	1.0201	0.7087
	TCN	0.9967	0.6988
	SaTCN	**0.9324**	**0.6547**
v	Forecasted	1.5605	1.0964
	Observed	1.1988	0.8633
	ConvLSTM	1.1567	0.8054
	HGAN	1.1356	0.7976
	TCN	1.0843	0.7532
	SaTCN	**1.0214**	**0.7321**
Overall	Forecasted	1.4264	1.0191
	Observed	1.0911	0.8311
	ConvLSTM	1.0004	0.8057
	HGAN	0.9889	0.8001
	TCN	0.9743	0.7956
	SaTCN	**0.9542**	**0.7569**

The bold values represent the smallest error values.

fields than the forecasted wind fields and the observed wind fields. As shown in Fig. 15, the historical wind field corrected by the SaTCN [see Fig. 15(d)], especially in the red box area, is visually more similar to the reanalysis wind field (Fig. 15(c)) than the forecasted wind field [see Fig. 15(a)] and the observed wind field [see Fig. 15(b)]. Fig. 16 describes the overall directions of the wind fields illustrated in Fig. 15. We utilize these corrected historical wind fields to conduct the Sanchi oil spill backtracking.

Fig. 17 presents the Sanchi oil spill backtracking results based on SaTCN corrected wind fields. The thousands of black dots represent the locations of oil spill particles at historical moments. Oil spill backtracking is conducted using these oil particles to simulate the historical drift trajectory. We define the coordinate average over all oil spill particles at the same time as the central location of the oil spills. The blue dots represent the central locations of the oil spills at historical moments. The blue triangle represents the backtracked location of the oil spill source and the red triangle represents the true location of the oil spill source.

Fig. 18 presents the Sanchi oil spill backtracking results based on different wind fields. To clearly show the historical trajectory, only the central locations of the oil spills at historical moments are exhibited in Fig. 18. By comparing different backtracking results in Fig. 18, we observe that the backtracking result based

TABLE VIII
AVERAGE CORRECTION RESULTS ON TWO TEST SETS IN THE OVERALL DIRECTION

Test set	Method	RMSE		MAE	
		Single input	Double inputs	Single input	Double inputs
Wind fields for Sanchi oil spill backtracking	Forecasted	1.1634	-	0.8797	-
	Observed	1.6687	-	1.2656	-
	ConvLSTM	1.1324	1.1028	0.8567	0.8453
	HGAN	1.1056	1.0845	0.8368	0.8256
	TCN	1.0889	1.0547	0.8189	0.8004
	SaTCN	1.0568	**0.9989**	0.8063	**0.7943**
Wind fields for Symphony oil spill backtracking	Forecasted	1.1049	-	0.8208	-
	Observed	0.9141	-	0.6947	-
	ConvLSTM	0.9121	0.9067	0.6834	0.6811
	HGAN	0.9100	0.9045	0.6801	0.6785
	TCN	0.8887	0.8745	0.6389	0.6223
	SaTCN	0.8211	**0.8078**	0.6045	**0.5804**

The bold values represent the smallest error values.

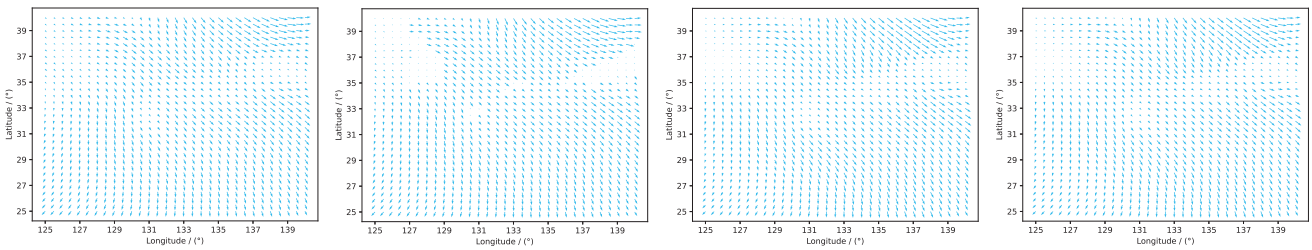

(a) (b) (c) (d)

Fig. 16. Wind directions of (a) the forecasted wind field, (b) the observed wind field, (c) the reanalysis wind field, and (d) the corrected historical wind field from the SaTCN on January 1, 2018 at 06:00 UTC.

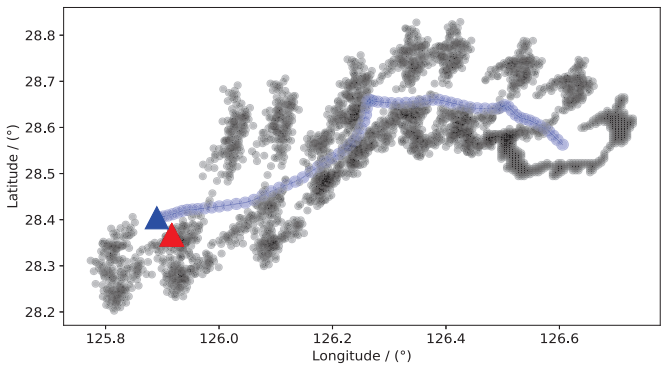

Fig. 17. Sanchi oil spill backtracking results based on SaTCN corrected wind fields. The black dots represent the oil spill locations at historical moments. The blue dots represent the central locations of the oil spills at historical moments. The blue triangle represents the backtracked location of the oil spill source and the red triangle represents the true location of the oil spill source.

on the SaTCN corrected wind fields are more close to the true oil spill source than those based on other wind fields.

To quantitatively evaluate the backtracking results of the Sanchi oil spill accident, we compute longitude errors, latitude errors, and distance errors based on the backtracking results in Fig. 18. Table IX presents the errors based on the basic backtracking methods and the WFCB methods. By comparing the backtracking errors, we can see that the errors of the WFCB methods are lower than those of the basic backtracking methods. The SaTCN based WFCB method has lower errors than other deep learning model based WFCB methods. Compared with the forecasted wind field based backtracking method, the SaTCN-based method reduces the distance error by 4187 m. The Sanchi oil spill backtracking experiments validate that the SaTCN based WFCB method is in favor of accurate backtracking results.

D. Symphony Oil Spill Backtracking

In this subsection, we validate the effectiveness of the WFCB method on the Symphony oil spill accident. The oil spill backtracking started from the time when the remote sensing image [shown in Fig. 12(a)] had been just acquired. At that time, the

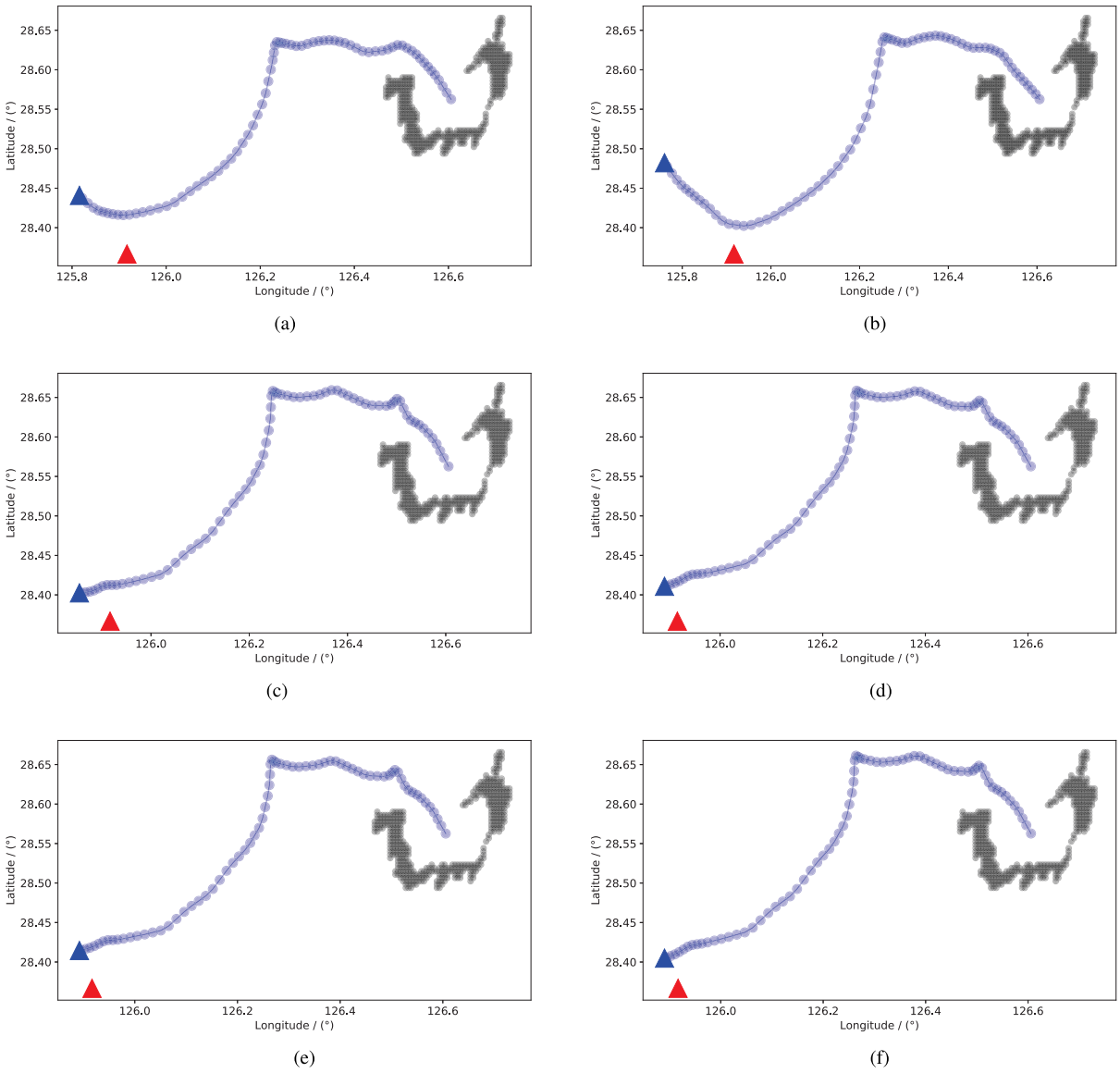

Fig. 18. Sanchi oil spill backtracking results based on different wind fields. The black dots represent the present oil spill locations. The blue dots represent the central locations of the oil spills at historical moments. The blue triangle represents the backtracked location of the oil spill source and the red triangle represents the true location of the oil spill source. (a) Backtracking based on forecasted wind fields from ECMWF. (b) Backtracking based on observed wind fields from CMEMS. (c) Backtracking based on corrected wind fields from ConvLSTM. (d) Backtracking based on corrected wind fields from HGAN. (e) Backtracking based on corrected wind fields from TCN. (f) Backtracking based on corrected wind fields from SaTCN.

TABLE IX
SOURCE LOCATION ERRORS OF SANCHI OIL SPILL BASED ON THE BASIC BACKTRACKING METHOD AND THE WFCB METHOD

Method	Wind Field	Longitude error x_e (°)	Latitude error y_e (°)	Distance error E_d (m)
Basic backtracking	Forecasted	1.0155×10^{-1}	7.5642×10^{-2}	8.5270×10^{3}
	Observed	1.5570×10^{-1}	1.1791×10^{-1}	1.3111×10^{4}
WFCB	ConvLSTM	6.2351×10^{-2}	$\mathbf{3.5785} \times 10^{-2}$	7.6224×10^{3}
	HGAN	2.5024×10^{-2}	4.4173×10^{-2}	5.5637×10^{3}
	TCN	$\mathbf{2.4544} \times 10^{-2}$	4.7892×10^{-2}	5.9115×10^{3}
	SaTCN	2.6173×10^{-2}	3.8935×10^{-2}	$\mathbf{4.3404} \times 10^{3}$

The bold values represent the smallest error values.

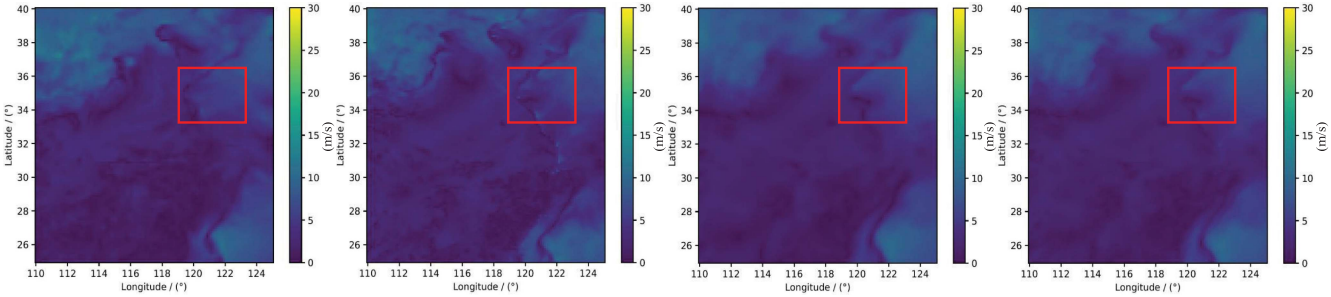

Fig. 19. Visual illustrations of (a) the forecasted wind field, (b) the observed wind field, (c) the reanalysis wind field, and (d) the corrected historical wind field from the SaTCN on April 27, 2021 at 06:00 UTC in the overall direction.

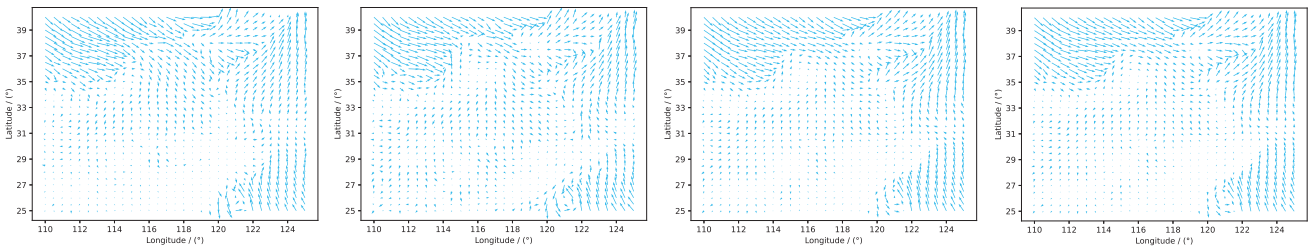

Fig. 20. Wind directions of (a) the forecasted wind field, (b) the observed wind field, (c) the reanalysis wind field, and (d) the corrected historical wind field from the SaTCN on April 27, 2021 at 06:00 UTC.

historical reanalysis wind fields are not available. As described in Section VI-C, the timely, accurate oil spill backtracking should be conducted based on the corrected historical wind fields.

Section VI-B has demonstrated that the proposed SaTCN has a better correction performance between April 1, 2021 at 00:00 UTC and May 1, 2021 at 18:00 UTC. The corrected historical wind fields are more similar to the reanalysis wind fields than the forecasted wind fields and the observed wind fields. As shown in Fig. 19, the historical wind field corrected by the SaTCN [see Fig. 19(d)], especially in the red box area, is visually more similar to the reanalysis wind field [see Fig. 19(c)] than the forecasted wind field [see Fig. 19(a)] and the observed wind field [see Fig. 19(b)]. Fig. 20 describes the overall directions of the wind fields illustrated in Fig. 19. We utilize these corrected historical wind fields for the Symphony oil spill backtracking.

Fig. 21 presents the Sanchi oil spill backtracking results based on SaTCN corrected wind fields. The thousands of black dots represent the present locations of oil spill particles. Oil spill backtracking is conducted using these oil particles to simulate the historical drift trajectory. The blue dots represent the central locations of the oil spills at historical moments. The blue triangle represents the backtracked location of the oil spill source and the red triangle represents the true location of the oil spill source.

Fig. 22 presents the Symphony oil spill backtracking results based on different wind fields. By comparing different backtracking results in Fig. 22, we observe that the backtracking results based on SaTCN corrected wind fields are more close to the true oil spill source than those based on other wind fields.

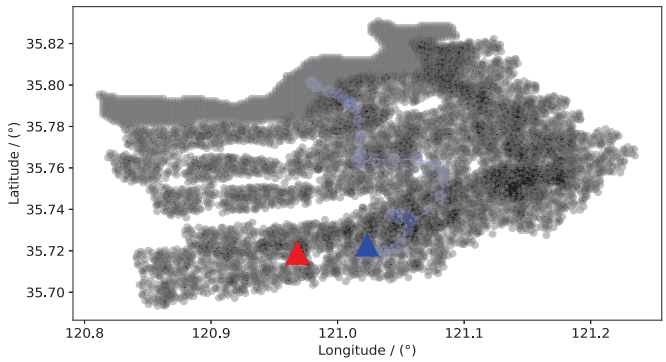

Fig. 21. Symphony oil spill backtracking results based on SaTCN corrected wind fields. The black dots represent the oil spill locations at historical moments. The blue dots represent the central locations of the oil spills at historical moments. The blue triangle represents the backtracked location of the oil spill source and the red triangle represents the true location of the oil spill source.

Table X presents the backtracking errors based on the basic backtracking methods and the WFCB methods. By comparing the backtracking errors, we can see that the errors of the WFCB methods are lower than those of the basic backtracking methods. The SaTCN-based WFCB method has lower errors than other deep learning model-based methods. Compared with the observed wind field-based backtracking method, the SaTCN-based method reduces the distance error by 1972 m. The backtracking experiments of the Symphony oil spill accident validate the effectiveness of the SaTCN-based WFCB method in accurate oil spill backtracking.

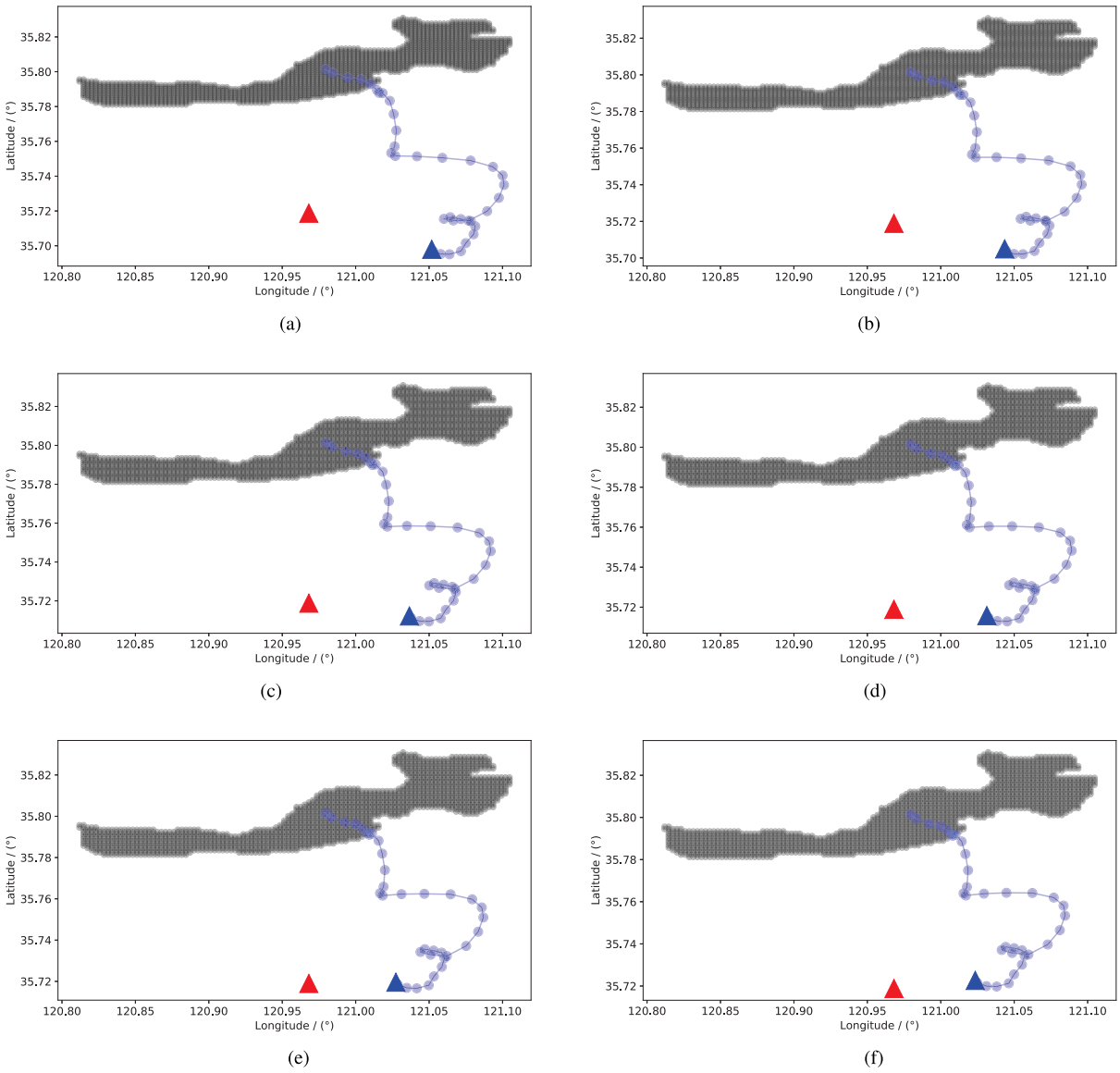

Fig. 22. Symphony oil spill backtracking results based on different wind fields. The black dots represent the present oil spill locations. The blue dots represent the central locations of the oil spills at historical moments. The blue triangle represents the backtracked location of the oil spill source and the red triangle represents the true location of the oil spill source. (a) Backtracking based on forecasted wind fields from NCEP. (b) Backtracking based on observed wind fields from CMEMS. (c) Backtracking based on corrected wind fields from ConvLSTM. (d) Backtracking based on corrected wind fields from HGAN. (e) Backtracking based on corrected wind fields from TCN. (f) Backtracking based on corrected wind fields from SaTCN.

TABLE X
SOURCE LOCATION ERRORS OF SYMPHONY OIL SPILL BASED ON THE BASIC BACKTRACKING METHOD AND THE WFCB METHOD

Method	Wind Field	Longitude error x_e (°)	Latitude error y_e (°)	Distance error E_d (m)
Basic backtracking	Forecasted	8.3105×10^{-2}	2.0784×10^{-2}	7.5109×10^{3}
	Observed	7.5432×10^{-2}	1.3793×10^{-2}	6.6480×10^{3}
WFCB	ConvLSTM	6.8487×10^{-2}	6.5845×10^{-3}	5.9011×10^{3}
	HGAN	6.3274×10^{-2}	3.1617×10^{-3}	5.4136×10^{3}
	TCN	5.9264×10^{-2}	$\mathbf{6.2109} \times 10^{-4}$	5.0520×10^{3}
	SaTCN	$\mathbf{5.4706} \times 10^{-2}$	3.7573×10^{-3}	$\mathbf{4.6761} \times 10^{3}$

The bold values represent the smallest error values.

VII. Concluding Remarks

A. Conclusion

In this article, we have developed an oil spill timely backtracking method oriented by wind field correction for locating pollution sources accurately. The wind field correction is conducted by an SaTCN framework, which is able to provide corrected historical wind fields that approximate the corresponding reanalysis wind fields. The corrected historical wind fields have enabled timely and accurate oil spill backtracking. Extensive experiments have validated the effectiveness of the proposed backtracking method in the Sanchi and Symphony oil spill accidents. Compared with the forecasted wind field-based backtracking method, the SaTCN-based method reduces the distance error by 4187 m in the Sanchi oil spill accident. Compared with the observed wind field-based backtracking method, the SaTCN-based method reduces the distance error by 1972 m in the Symphony oil spill accident.

B. Limitations

There are various issues that may influence the fate of oil spills on the sea surface. Our work has focused on one major issue of wind fields and managed to increase the accuracy of oil spill backtracking by developing deep learning method for improving the accuracy of the wind field data. The other issues such as the type of spilled oil and the effects of oil weathering are not considered in our current work.

C. Future Work

As with any new approach, there are some unresolved issues that may present challenges over time. Our future research will include the development of a more comprehensive oil spill backtracking model [11] that can account for the movement of oil spills considering the type of spilled oil and the effects of oil weathering. In addition, using a regional marine circulation model instead of the global model HYCOM may provide current fields with higher temporal and spatial resolutions, which would improve the backtracking accuracy effectively.

References

[1] C. Dearden, T. Culmer, and R. Brooke, "Performance measures for validation of oil spill dispersion models based on satellite and coastal data," *IEEE J. Ocean. Eng.*, vol. 47, no. 1, pp. 126–140, Jan. 2022.

[2] Y. Wang et al., "Environmental impact and recovery of the Bohai Sea following the 2011 oil spill," *Environ. Pollut.*, vol. 263, 2020, Art. no. 114343.

[3] C. Bayındır, J. D. Frost, and C. F. Barnes, "Assessment and enhancement of SAR noncoherent change detection of sea-surface oil spills," *IEEE J. Ocean. Eng.*, vol. 43, no. 1, pp. 211–220, Jan. 2018.

[4] P. Ren, M. Xu, Y. Yu, F. Chen, X. Jiang, and E. Yang, "Energy minimization with one dot fuzzy initialization for marine oil spill segmentation," *IEEE J. Ocean. Eng.*, vol. 44, no. 4, pp. 1102–1115, Oct. 2018.

[5] B. Zhang, X. Li, W. Perrie, and O. Garcia-Pineda, "Compact polarimetric synthetic aperture radar for marine oil platform and slick detection," *IEEE Trans. Geosci. Remote Sens.*, vol. 55, no. 3, pp. 1407–1423, Mar. 2017.

[6] H. Zheng, C. Gou, A. Khenchaf, Y. Wang, and Y. Zhang, "Retrieving oil-water mixture ratios of marine oil spills from L-band SAR imagery," *IEEE Trans. Geosci. Remote Sens.*, vol. 60, pp. 1–11, 2022.

[7] A. Trucco et al., "Compounding approaches for wind prediction from underwater noise by supervised learning," *IEEE J. Ocean. Eng.*, vol. 47, no. 4, pp. 1172–1187, Oct. 2022.

[8] P. Keramea, K. Spanoudaki, G. Zodiatis, G. Gikas, and G. Sylaios, "Oil spill modeling: A critical review on current trends, perspectives, and challenges," *J. Mar. Sci. Eng.*, vol. 9, no. 2, 2021, Art. no. 181.

[9] G. Zodiatis et al., "Oil spill forecasting (prediction)," *J. Mar. Res.*, vol. 75, no. 6, pp. 923–953, 2017.

[10] R. Fernandes, A. Necci, and E. Krausmann, "Model(s) for the dispersion of hazardous substances in floodwaters for rapid-n," 2022.

[11] M. L. Spaulding, "State of the art review and future directions in oil spill modeling," *Mar. Pollut. Bull.*, vol. 115, no. 1/2, pp. 7–19, 2017.

[12] C. Ambjorn, O. Liungman, J. Mattsson, and B. Håkansson, "Seatrack Web: The HELCOM tool for oil spill prediction and identification of illegal polluters," in *Proc. IEEE/OES Baltic Int. Symp.*, 2014, pp. 155–183.

[13] T. Parviainen, S. Kuikka, and P. Haapasaari, "Enhancing science-policy interface in marine environmental governance: Oil spill response models as boundary objects in the Gulf of Finland, Baltic Sea," *Mar. Policy*, vol. 135, 2022, Art. no. 104863.

[14] E. Howlett, K. Jayko, T. Isaji, P. Anid, G. Mocke, and F. Smit, "Marine forecasting and oil spill modeling in Dubai and the Gulf region," in *Proc. 7th Int. Conf. Coastal Port Eng. Developing Countries*, 2008, pp. 1–12.

[15] A. Abascal, S. Castanedo, V. Fernandez, M. Ferrer, and R. Medina, "Oil spill trajectory forecasting and backtracking using surface currents from high-frequency (HF) radar technology," in *Proc. OCEANS IEEE-Spain*, 2011, pp. 1–8.

[16] A. J. Abascal, S. Castanedo, V. Fernández, and R. Medina, "Backtracking drifting objects using surface currents from high-frequency (HF) radar technology," *Ocean Dyn.*, vol. 62, no. 7, pp. 1073–1089, 2012.

[17] K. Al-Salem, Y. Y. Alosairi, and A. A. Al-Rashed, "Development of a backtracking numerical model for offshore oil spills," *J. Eng. Res.*, vol. 5, no. 1, pp. 1–22, 2017.

[18] J. Janeiro, A. Neves, F. Martins, and P. Relvas, "Integrating technologies for oil spill response in the SW Iberian coast," *J. Mar. Syst.*, vol. 173, pp. 31–42, 2017.

[19] A. J. Abascalet al., "Operational oil spill trajectory modelling using HF radar currents: A northwest European continental shelf case study," *Mar. Pollut. Bull.*, vol. 119, no. 1, pp. 336–350, 2017.

[20] N. F. Putman, F. A. Abreu-Grobois, I. Iturbe-Darkistade, E. M. Putman, P. M. Richards, and P. Verley, "Deepwater horizon oil spill impacts on sea turtles could span the Atlantic," *Biol. Lett.*, vol. 11, no. 12, 2015, Art. no. 20150596.

[21] S. Tian, X. Huang, and H. Li, "A new method to locate oil spill origin with modified Lagrangian model-A case study of pl19-3 oil spill accident," in *Proc. IEEE Int. Geosci. Remote Sens. Symp.*, 2016, pp. 4477–4480.

[22] V. Suneel, A. Ciappa, and P. Vethamony, "Backtrack modeling to locate the origin of tar balls depositing along the West coast of India," *Sci. Total Environ.*, vol. 569, pp. 31–39, 2016.

[23] S. Tian, X. Huang, and H. Li, "A new method to calibrate Lagrangian model with ASAR images for oil slick trajectory," *Mar. Pollut. Bull.*, vol. 116, no. 1/2, pp. 95–102, 2017.

[24] H. Chen, "Performance of a simple backtracking method for marine oil source searching in a 3D ocean," *Mar. Pollut. Bull.*, vol. 142, pp. 321–334, 2019.

[25] A. C. Ciappa, "Reverse trajectory study of oil spill risk in cyclades islands of the Aegean Sea," *Regional Stud. Mar. Sci.*, vol. 41, 2021, Art. no. 101580.

[26] D. P. Deeet al., "The era-interim reanalysis: Configuration and performance of the data assimilation system," *Quart. J. Roy. Meteorological Soc.*, vol. 137, no. 656, pp. 553–597, 2011.

[27] I. Staffell and S. Pfenninger, "Using bias-corrected reanalysis to simulate current and future wind power output," *Energy*, vol. 114, pp. 1224–1239, 2016.

[28] C. Mears, T. Lee, L. Ricciardulli, X. Wang, and F. Wentz, "Improving the accuracy of the cross-calibrated multi-platform (CCMP) ocean vector winds," *Remote Sens.*, vol. 14, no. 17, 2022, Art. no. 4230.

[29] F. Cassola and M. Burlando, "Wind speed and wind energy forecast through Kalman filtering of numerical weather prediction model output," *Appl. Energy*, vol. 99, pp. 154–166, 2012.

[30] C. P. Sweeney, P. Lynch, and P. Nolan, "Reducing errors of wind speed forecasts by an optimal combination of post-processing methods," *Meteorological Appl.*, vol. 20, no. 1, pp. 32–40, 2013.

[31] A. M. Ishak, R. Remesan, P.K. Srivastava, T. Islam, and D. Han, "Error correction modelling of wind speed through hydro-meteorological parameters and mesoscale model: A hybrid approach," *Water Resour. Manage.*, vol. 27, no. 1, pp. 1–23, 2013.

[32] P. Lauret, H. M. Diagne, and M. David, "A neural network post-processing approach to improving NWP solar radiation forecasts," *Energy Procedia*, vol. 57, pp. 1044–1052, 2014.

[33] L. Zjavka, "Wind speed forecast correction models using polynomial neural networks," *Renewable Energy*, vol. 83, pp. 998–1006, 2015.
[34] Y. Liu, Y. Wang, L. Li, S. Han, and D. Infield, "Numerical weather prediction wind correction methods and its impact on computational fluid dynamics based wind power forecasting," *J. Renewable Sustain. Energy*, vol. 8, no. 3, 2016, Art. no. 033302.
[35] S. Buhan, Y. Özkazanç, and I. Çadırcı, "Wind pattern recognition and reference wind mast data correlations with NWP for improved wind-electric power forecasts," *IEEE Trans. Ind. Inform.*, vol. 12, no. 3, pp. 991–1004, Jun. 2016.
[36] X. Chen, W. Huang, and M. C. Haller, "A novel scheme for extracting sea surface wind information from rain-contaminated x-band marine radar images," *IEEE J. Sel. Topics Appl. Earth Observ. Remote Sens.*, vol. 14, pp. 5220–5234, 2021.
[37] R. Tang, Y. Ning, C. Li, W. Feng, Y. Chen, and X. Xie, "Numerical forecast correction of temperature and wind using a single-station single-time spatial lightGBM method," *Sensors*, vol. 22, no. 1, 2022, Art. no. 193.
[38] L. Ye, B. Dai, Z. Li, M. Pei, Y. Zhao, and P. Lu, "An ensemble method for short-term wind power prediction considering error correction strategy," *Appl. Energy*, vol. 322, 2022, Art. no. 119475.
[39] Y. Wang, T. Gao, Z. Han, and Q. Liu, "Impacts of wind-field correction on the numerical simulation of storm-surge inundation during typhoon "Rammasun"," *Estuarine, Coastal Shelf Sci.*, vol. 196, pp. 198–206, 2017.
[40] S. Kotal and S. Bhattacharya, "Improvement of wind field forecasts for tropical cyclones over the north Indian Ocean," *Trop. Cyclone Res. Rev.*, vol. 9, no. 1, pp. 53–66, 2020.
[41] L. Han et al., "A deep learning method for bias correction of ECMWF 24–240 h forecasts," *Adv. Atmospheric Sci.*, vol. 38, no. 9, pp. 1444–1459, 2021.
[42] J. Zhang, P. Wu, X. Xu, M. Han, and B. Pan, "PCS-LSTM: A hybrid deep learning model for multi-stations joint temperature prediction based on periodicity and closeness," *Neurocomputing*, vol. 501, pp. 151–161, 2022.
[43] X. Shi, Z. Chen, H. Wang, D.-Y. Yeung, W.-K. Wong, and W.-c. Woo, "Convolutional LSTM network: A machine learning approach for precipitation nowcasting," in *Proc. Adv. Neural Inf. Process. Syst.*, 2015, pp. 802–810.
[44] Y. Li, W. Huang, X. Lyu, S. Liu, Z. Zhao, and P. Ren, "An adversarial learning approach to forecasted wind field correction with an application to oil spill drift prediction," *Int. J. Appl. Earth Observ. Geoinformation*, vol. 112, 2022, Art. no. 102924.
[45] C. Lea, M. D. Flynn, R. Vidal, A. Reiter, and G. D. Hager, "Temporal convolutional networks for action segmentation and detection," in *Proc. IEEE Conf. Comput. Vis. Pattern Recognit.*, 2017, pp. 156–165.
[46] A. J. Abascal, S. Castanedo, R. Minguez, R. Medina, Y. Liu, and R. H. Weisberg, "Stochastic lagrangian trajectory modeling of surface drifters deployed during the deepwater horizon oil spill," in *Proc. 38th AMOP Tech. Seminar; Environ.*, 2015, pp. 77–91.
[47] A. Toz and B. Koseoglu, "Trajectory prediction of oil spill with Pisces 2 around Bay of Izmir, Turkey," *Mar. Pollut. Bull.*, vol. 126, pp. 215–227, 2018.
[48] T. Nordam, C. Beegle-Krause, J. Skancke, R. Nepstad, and M. Reed, "Improving oil spill trajectory modelling in the Arctic," *Mar. Pollut. Bull.*, vol. 140, pp. 65–74, 2019.
[49] M. Nogueira, "Inter-comparison of era-5, era-interim and GPCP rainfall over the last 40 years: Process-based analysis of systematic and random differences," *J. Hydrol.*, vol. 583, 2020, Art. no. 124632.
[50] L. Shi, N. Liang, X. Xu, T. Li, and Z. Zhang, "SA-JSTN: Self-attention joint spatiotemporal network for temperature forecasting," *IEEE J. Sel. Topics Appl. Earth Observ. Remote Sens.*, vol. 14, pp. 9475–9485, 2021.
[51] X. Wang, R. Girshick, A. Gupta, and K. He, "Non-local neural networks," in *Proc. IEEE Conf. Comput. Vis. Pattern Recognit.*, 2018, pp. 7794–7803.
[52] S. Ji, W. Xu, M. Yang, and K. Yu, "3D convolutional neural networks for human action recognition," *IEEE Trans. Pattern Anal. Mach. Intell.*, vol. 35, no. 1, pp. 221–231, Jan. 2013.
[53] H. Li, S. Gao, G. Liu, D. Guo, C. Grecos, and P. Ren, "Visual prediction of typhoon clouds with hierarchical generative adversarial networks," *IEEE Geosci. Remote Sens. Lett.*, vol. 17, no. 9, pp. 1478–1482, Sep. 2020.

Yongqing Li received the B.Eng. degree in electronic information engineering, the M.Eng. degree in information and communication engineering, and the Ph.D. degree in control science and engineering from the China University of Petroleum (East China), Qingdao, China, in 2013, 2016, and 2023, respectively.

He is currently a Lecturer with the School of Data Science, Qingdao University of Science and Technology, Qingdao, China. His research interests include oil spill detection, drift prediction, and backtracking.

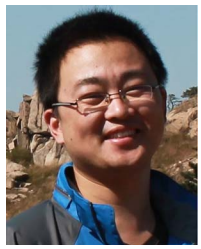

Xinrong Lyu received the bachelor's degree in electronic engineering and the doctoral degree in pattern recognition and intelligent system from Xidian University, Xi'an, China, in 2004 and 2009, respectively.

He is currently an Associate Professor with the College of Oceanography and Space Informatics, China University of Petroleum (East China), Qingdao, China. His research interests include machine learning and oil spill detection.

Peng Ren (Senior Member, IEEE) received the B.Eng. and M.Eng. degrees in electronic engineering from the Harbin Institute of Technology, Harbin, China, and the Ph.D. degree in computer science from the University of York, York, U.K., in 2003, 2005, and 2010, respectively.

He is currently a Professor with the College of Oceanography and Space Informatics, China University of Petroleum (East China), Qingdao, China. His research interests include remote sensing and oceanic information processing.

Dr. Ren was the recipient of the K. M. Scott Prize from the University of York in 2011 and the Eduardo Caianiello Best Student Paper Award at the 18th International Conference on Image Analysis and Processing in 2015, as one coauthor.